

## EVIDENCE FOR DISK–STELLAR MUTUAL INCLINATIONS AND RECURRENT ECLIPSES IN THE YOUNG AND MASSIVE GW ORI TRIPLE SYSTEM

IAN CZEKALA,<sup>1,\*</sup> SEAN M. ANDREWS,<sup>2</sup> GUILLERMO TORRES,<sup>2</sup> JOSEPH E. RODRIGUEZ,<sup>2</sup> ERIC L. N. JENSEN,<sup>3</sup>  
KEIVAN G. STASSUN,<sup>4,5</sup> DAVID W. LATHAM,<sup>2</sup> DAVID J. WILNER,<sup>2</sup> MICHAEL B. LUND,<sup>6</sup> RUDOLF B. KUHN,<sup>7</sup>  
DANIEL J. STEVENS,<sup>8</sup> ROBERT J. SIVERD,<sup>9</sup> DAVID JAMES,<sup>10</sup> B. SCOTT GAUDI,<sup>8</sup> KONSTANTIN N. GRANKIN,<sup>11</sup>  
BENJAMIN J. SHAPPEE,<sup>12,13</sup> KRZYSZTOF Z. STANEK,<sup>8,14</sup> THOMAS W.-S. HOLOIEN,<sup>8,14,15</sup> CHRISTOPHER S. KOCHANEK,<sup>8,14</sup>  
AND JOSE L. PRIETO<sup>16,17</sup>

<sup>1</sup>*Kavli Institute for Particle Astrophysics and Cosmology, Stanford University, 452 Lomita Mall, Stanford, CA 94305, USA*

<sup>2</sup>*Harvard-Smithsonian Center for Astrophysics, 60 Garden Street, Cambridge, MA 02138, USA*

<sup>3</sup>*Department of Physics and Astronomy, Swarthmore College, 500 College Avenue, Swarthmore, PA 19081, USA*

<sup>4</sup>*Department of Physics and Astronomy, Vanderbilt University, Nashville, TN 37235, USA*

<sup>5</sup>*Department of Physics, Fisk University, Nashville, TN 37208, USA*

<sup>6</sup>*Department of Physics and Astronomy, Vanderbilt University, 6301 Stevenson Center, Nashville, TN 37235, USA*

<sup>7</sup>*South African Astronomical Observatory, P.O. Box 9, Observatory 7935, South Africa*

<sup>8</sup>*Department of Astronomy, The Ohio State University, Columbus, OH 43210, USA*

<sup>9</sup>*Las Cumbres Observatory Global Telescope Network, 6740 Cortona Drive, Suite 102, Santa Barbara, CA 93117, USA*

<sup>10</sup>*Astronomy Department, University of Washington, Box 351580, Seattle, WA 98195, USA*

<sup>11</sup>*Crimean Astrophysical Observatory, pos. Nauchnyi, Crimea, 298409 Russia*

<sup>12</sup>*Carnegie Observatories, 813 Santa Barbara Street, Pasadena, CA 91101, USA*

<sup>13</sup>*Hubble, Carnegie-Princeton Fellow*

<sup>14</sup>*Center for Cosmology and AstroParticle Physics (CCAPP), The Ohio State University, 191 W. Woodruff Ave., Columbus, OH 43210, USA*

<sup>15</sup>*US Department of Energy Computational Science Graduate Fellow*

<sup>16</sup>*Nucleo de Astronomia de la Facultad de Ingenieria, Universidad Diego Portales, Av. Ejercito 441, Santiago, Chile*

<sup>17</sup>*Millennium Institute of Astrophysics, Santiago, Chile*

### ABSTRACT

We present spatially and spectrally resolved Atacama Large Millimeter/submillimeter Array (ALMA) observations of gas and dust in the disk orbiting the pre-main sequence triple GW Ori. We forward-model the <sup>13</sup>CO and C<sup>18</sup>O  $J=2-1$  transitions to put precise constraint on the total stellar mass of  $5.29 \pm 0.09 M_{\odot}$ , and disk inclination of  $i_{\text{disk}} = 137.6 \pm 2.0^{\circ}$ . We use 35 years of optical radial velocity monitoring and spectroscopic dentangling techniques to reveal GW Ori as a near equal-flux double-lined spectroscopic binary. Combining the measurements from these two datasets yields a precise constraint on the stellar masses of XX. We publish a light curve with a 30-year baseline that shows several eclipse events. We show that this precise mass is consistent with the predictions of leading pre-main sequence evolutionary models based upon its observed photospheric properties. We put constraints on the orbital configuration of the triple system within the massive disk and discuss this in the context of star and planet formation.

*Keywords:* protoplanetary disks – stars: fundamental parameters – stars: pre-main sequence – stars: individual (GW Ori)

## 1. INTRODUCTION

Pre-main sequence stars in multiple systems—for which it is possible to precisely measure their fundamental stellar properties—can serve as touchstones for understanding the final stages of stellar formation and the conditions under which planetary systems are assembled. While recent decades have seen steady progress in understanding binary formation in general, lingering uncertainties still remain about the characteristics of young close-in spectroscopic binaries and higher order systems (Duchêne & Kraus 2013). GW Ori was one of the first T Tauri stars to be revealed as a spectroscopic binary (Mathieu et al. 1991), with a composite G spectral type of and an orbital period of 240 days. Long term radial velocity monitoring hinted at the presence of a third body in the system with a period of  $\sim 10$  years, and was subsequently confirmed by infrared interferometry (Berger et al. 2011). GW Ori is a member of the  $\lambda$  Orionis star forming complex, a young OB association (Dolan 2000; Dolan & Mathieu 2001, 2002) in Orion. The most recent and precise measurements of the distance to Orion Nebula Complex is a VLBA parallax measurement of  $388 \pm 5$  pc (Kounkel et al. 2017), which we adopt as the distance to GW Ori.

A reservoir of circumstellar material orbiting GW Ori was inferred from near and far-infrared emission in excess of the stellar photosphere (Mathieu et al. 1991), and was subsequently confirmed by a strong single-dish submillimeter detection of the dust continuum, suggesting a massive circumstellar disk ( $M_{\text{disk}} \gtrsim 0.1 M_{\odot}$ ; Mathieu et al. 1995). Quasi-periodic photometric dimmings of GW Ori have been observed to occur on  $\sim 100$  day timescales, and are suspected to be due from material in the circumstellar disk occulting the primary star (Shevchenko et al. 1992, 1998), although the fact that edge-on orbital inclinations are ruled out complicates this interpretation. **Need to introduce this in proper chronological order.**

Mid-infrared spectroscopic observations of GW Ori detected CO fundamental emission with line profiles that have both a narrow and broad component, requiring a complicated emission region and temperature structure in the inner disk (Najita et al. 2003). Fang et al. (2014) compile several epochs of spectral energy distributions (SEDs) spanning decades and find that the mid-infrared emission is variable on the timescale of years. The SED and its variability can be explained by a gapped disk with changes in the structure of the inner disk.

Spatially and spectrally resolved sub-millimeter observations of molecular gas lines in protoplanetary disks can be used to reconstruct the disk velocity field and independently measure the total stellar mass of the system

(e.g., Rosenfeld et al. 2012; Czekala et al. 2015, 2016). Here we report the first resolved sub-mm observations of the GW Ori system with the ALMA interferometer, which reveal the presence of a large and massive protoplanetary disk. We forward-model the protoplanetary disk to infer the total mass of the enclosed stars. We re-analyze 35 years of optical spectra to reveal GW Ori as a low semi-amplitude spectroscopic binary and derive updated orbital constraints on GW Ori A, B, and C. We combine these mass constraints with measurements of the photospheric properties of A and B to evaluate their agreement with leading pre-main sequence models. **Do we detect spectroscopic light from C?** We also present a 30-year baseline light curve, which includes the detection of several quasi-periodic eclipse events. We also discuss the structure and orientation of the protoplanetary disk with respect to the putative orbital inclinations of the stellar components and place the quasi-period eclipsing nature of GW Ori in the context of other recently discovered “dipper” stars (e.g., Ansdel et al. 2016a,b).

## 2. OBSERVATIONS AND DATA REDUCTION

### 2.1. Millimeter Interferometry

GW Ori was observed with the ALMA interferometer on 2015 May 14 (program ID 2012.1.00496.S), with 37 of the 12 m main array antennas configured to span baselines of 23–558 m. The double sideband Band 6 receivers were employed in dual polarization mode, and the ALMA correlator was set up to process data in 4 spectral windows (SPWs). Two of these SPWs, centered at 220.426 and 230.450 GHz to observe the nearby  $^{13}\text{CO}$  and  $^{12}\text{CO}$   $J=2-1$  transitions (at rest frequencies of 220.399 and 230.538 GHz, respectively), covered 234 MHz of bandwidth in 3840 channels (a 61 kHz channel spacing). One other sampled 469 MHz around 219.763 GHz to observe the nearby  $\text{C}^{18}\text{O}$   $J=2-1$  transition (at rest frequency 219.560 GHz) with 3840 channels (a 122 kHz channel spacing). The last SPW sampled the continuum in a 1.875 GHz range around 231.956 GHz using 128 coarse channels (a 15.625 MHz channel spacing).

The observations cycled between GW Ori and the quasar J0510+1800 with a 7 minute cadence. The quasar J0423-0120 and Ganymede were observed as bandpass and flux calibration sources, respectively, at the start of the execution block. The total on-source integration time for GW Ori was 16 minutes. The observing conditions were typical for Band 6 projects, with a precipitable water vapor level around 1.1 mm.

The visibility data were calibrated with standard procedures using the CASA software package (v4.4). The raw, observed visibility phases were adjusted based on the contemporaneous measurements of water vapor ra-

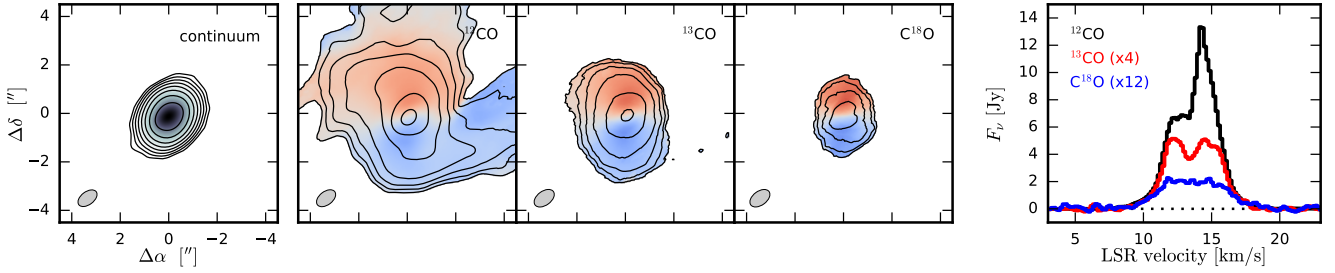


**Figure 1.** (left) A 226 GHz continuum image. Contours start at  $5 \times$  the RMS noise level and increase by factors of 2. The synthesized beam geometry is shown in the lower left corner. (middle, left to right) Maps of the  $^{12}\text{CO}$ ,  $^{13}\text{CO}$ , and  $\text{C}^{18}\text{O}$  velocity-integrated intensities (contours, starting at 10, 3, and 3 $\times$  the RMS noise levels, respectively, and increasing by factors of 2) overlaid on the intensity-weighted projected velocities (color-scale). Note the prominent molecular cloud contamination in the  $^{12}\text{CO}$  map (see also Fig. 2). (right) Spatially integrated spectra (inside the same CLEAN mask, and smoothed with an  $0.85 \text{ km s}^{-1}$  Hanning kernel) for each CO line.

diameters, flagged when applicable, and then the bandpass shape in (and between) each SPW was calibrated based on the observations of J0423-0120. The absolute amplitude scale was determined based on the observations of Ganymede. The complex gain behavior of the array and atmosphere was corrected based on the repeated observations of J0510+1800. The calibrated visibilities showed a strong continuum signal, suggesting that self-calibration could significantly improve the data quality. An initial model based on a preliminary continuum image was used for two rounds of phase-only self-calibration (on 30 s, then 6 s intervals) and one additional round that included the amplitudes (on a 7 minute scan interval). This self-calibration reduced the RMS noise level in the continuum by a factor of  $\sim 40$ . After applying the self-calibration tables to the entire dataset (channel by channel), we parsed out data products for each individual emission tracer of interest. A set of continuum visibilities was constructed by spectrally averaging the line-free channels in each SPW into  $\sim 125 \text{ MHz}$  increments. The spectral visibilities for the  $^{12}\text{CO}$ ,  $^{13}\text{CO}$ , and  $\text{C}^{18}\text{O}$  lines were continuum-subtracted and regridded into  $170 \text{ m s}^{-1}$ -wide channels in the LSRK restframe over a  $\sim 10 \text{ km s}^{-1}$  range around the line centers.

These fully reduced visibility sets were then imaged by Fourier inversion assuming a Briggs (robust=0.5) weighting scheme and deconvolution with the standard CLEAN algorithm. Some basic image properties for the synthesized continuum image and spectral line image cubes are listed in Table 1. The continuum and spectral line moment maps are shown together in Figure 1, along with a comparison of the integrated spectra. The channel maps for individual lines are compiled in Figure 2.

The 226 GHz (1.3 mm) continuum map shows a bright (flux density = 202 mJy), compact but marginally resolved (deconvolved Gaussian FWHM  $\approx 0.^{\prime\prime}9$ ) source centered on the GW Ori stellar system, with a peak intensity of  $67 \text{ mJy beam}^{-1}$  ( $\text{S/N} \approx 1200$ ). A crude es-

timate of the emission geometry (from a Gaussian fit to the visibilities) suggests an inclination of  $35\text{--}40^\circ$  from face-on, with the major axis oriented  $\sim 170^\circ$  E of N.

The CO isotopologue channel maps reveal bright (integrated intensities of 41.8, 5.7, and  $0.8 \text{ Jy km s}^{-1}$  for  $^{12}\text{CO}$ ,  $^{13}\text{CO}$ , and  $\text{C}^{18}\text{O}$ , respectively) and extended (FWHM  $\sim 2.^{\prime}5$ ) emission that is clearly in rotation around the continuum centroid, spanning a projected velocity range of  $\pm 5 \text{ km s}^{-1}$  from the line center. The line emission is blueshifted to the south and redshifted to the north, consistent with the orientation estimated from the continuum emission. The peak intensities for each line are  $\sim 800$ , 290, and  $55 \text{ mJy beam}^{-1}$  in the brightest channels (peak S/N  $\approx 130$ , 35, and 14) for  $^{12}\text{CO}$ ,  $^{13}\text{CO}$ , and  $\text{C}^{18}\text{O}$ , respectively. The  $^{12}\text{CO}$  channel maps show some clear evidence for structured contamination from the surrounding molecular cloud, particularly as a streamer to the west at LSRK velocities  $\sim 11\text{--}13 \text{ km s}^{-1}$  and some diffuse clumps to the north around  $13\text{--}14 \text{ km s}^{-1}$ . Those features are much fainter, but still present, in  $^{13}\text{CO}$  emission; they are not apparent in the  $\text{C}^{18}\text{O}$  maps.

**Table 1.** ALMA Image Properties

	RMS	
	beam dimensions	$\text{mJy beam}^{-1}$
226 GHz continuum	$0.^{\prime\prime}88 \times 0.^{\prime\prime}54, 126^\circ$	0.055
$^{12}\text{CO } J=2-1$	$0.^{\prime\prime}89 \times 0.^{\prime\prime}56, 126^\circ$	6
$^{13}\text{CO } J=2-1$	$0.^{\prime\prime}93 \times 0.^{\prime\prime}59, 126^\circ$	8
$\text{C}^{18}\text{O } J=2-1$	$0.^{\prime\prime}92 \times 0.^{\prime\prime}58, 126^\circ$	5

NOTE—The RMS noise levels recorded for the spectral line cubes correspond to the values per  $170 \text{ m s}^{-1}$  channel.

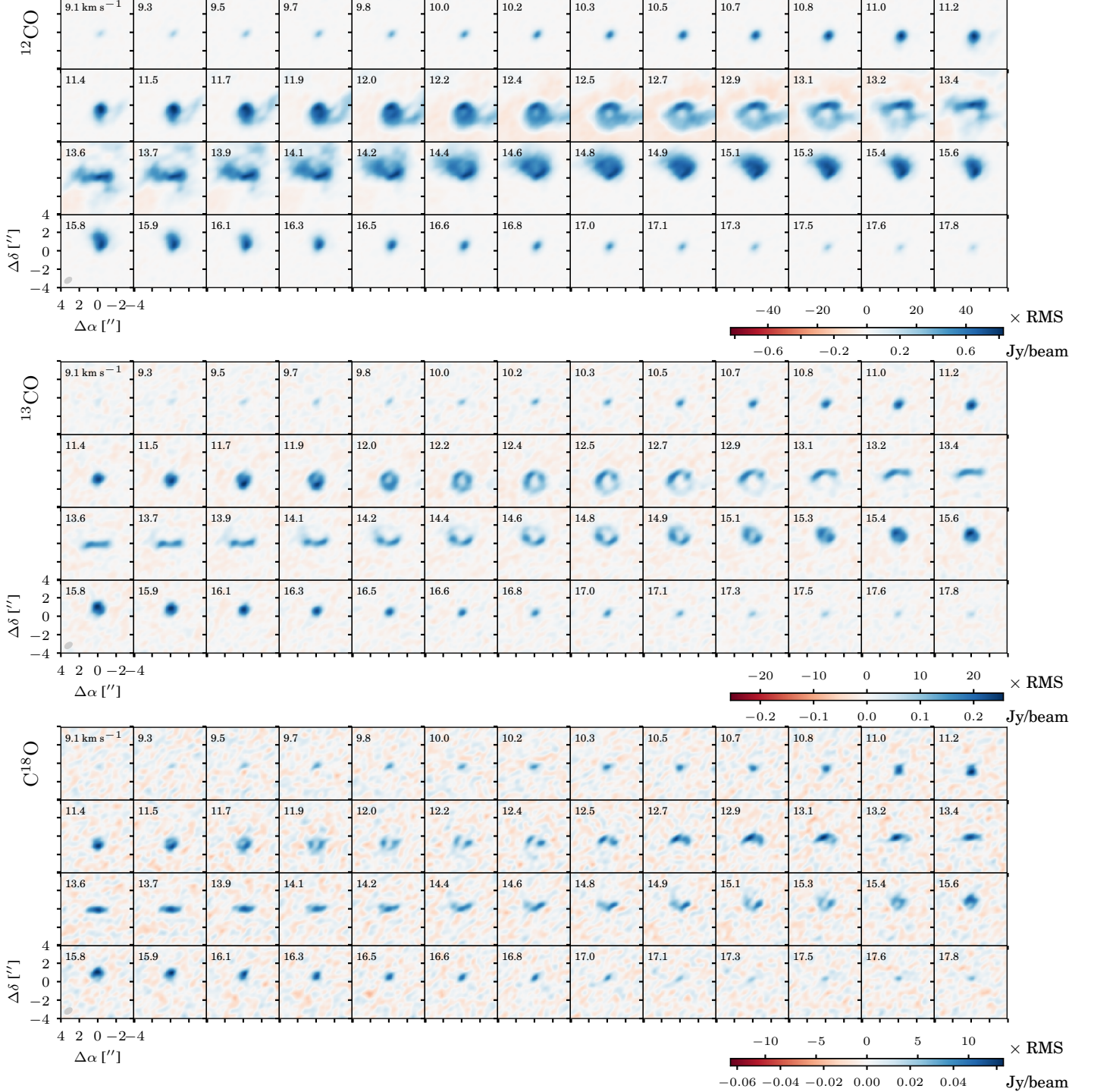


**Figure 2.** Channel maps of the  $^{12}\text{CO}$ ,  $^{13}\text{CO}$ , and  $\text{C}^{18}\text{O}$  (*from top to bottom*) line emission from the GW Ori disk. Each channel represents the emission in a  $170\text{ m s}^{-1}$ -wide velocity bin. LSRK velocities are indicated in the upper left, and synthesized beam sizes in the lower left, or each panel. Scale bars are provided at the bottom right of each set of channel maps.

## 2.2. Optical Spectroscopy

GW Ori was monitored spectroscopically at the Harvard-Smithsonian Center for Astrophysics for more than 35 years, beginning in 1981 November. A to-

tal of 208 spectra were gathered through 2009 April using three nearly identical echelle spectrographs (Digital Speedometers, DS; now decommissioned) with a resolving power of  $R \approx 35,000$  mounted on three different telescopes: the 1.5m Tillinghast reflector at the

Fred L. Whipple Observatory (Mount Hopkins, AZ), the 4.5m-equivalent Multiple Mirror Telescope (also on Mount Hopkins) before conversion to a monolithic mirror, and occasionally on the 1.5m Wyeth reflector at the Oak Ridge Observatory (in the town of Harvard, MA). Each instrument was equipped with an intensified photon-counting Reticon detector limiting the output to a single echelle order 45 Å wide, which was centered on the region of the Mg I b triplet at 5187 Å (see Latham 1992). The signal-to-noise ratios of these observations range from 14 to 59 per resolution element of  $8.5 \text{ km s}^{-1}$ . Wavelength calibrations were based on exposures of a Thorium-Argon lamp taken before and after each science exposure. Reductions were performed with a dedicated pipeline, and the zero-point of the velocities was monitored regularly by means of exposures of the evening and morning twilight sky. A further 80 spectra of GW Ori were collected with the Tillinghast Reflector Echelle Spectrograph (TRES; Fűrész 2008), a bench-mounted, fiber-fed echelle instrument mounted on the 1.5m Tillinghast reflector with a resolving power of  $R \approx 44,000$  and delivering 51 orders covering the wavelength interval 3900–9100 Å. These observations were made between 2010 November and 2016 April. Signal-to-noise ratios at 5200 Å range from 28 to 195 per resolution element of  $6.8 \text{ km s}^{-1}$ . Wavelength calibration was carried out as above, and reductions were performed as described by Buchhave et al. (2010). Radial-velocity standard stars were observed each night to monitor the zero point and place it on the same system as the DS observations to within  $\sim 0.1 \text{ km s}^{-1}$ .

All of our spectra appear single-lined. Radial velocities (RVs) were measured by cross-correlation using the IRAF<sup>1</sup> task XCSAO (Kurtz & Mink 1998), with templates taken from a large library of calculated spectra based on model atmospheres by R. L. Kurucz (see Nordstroem et al. 1994; Latham et al. 2002). These synthetic templates cover a 300 Å region centered on the Mg I b triplet, and are available for a wide range of effective temperatures ( $T_{\text{eff}}$ ), surface gravities ( $\log g$ ), metallicities ([Fe/H]), and rotational broadenings ( $v \sin i$  when seen in projection). The optimal template was selected by running grids of cross-correlations over broad ranges in the template parameters, as described by Torres et al. (2002), seeking the best match as measured by the peak cross-correlation coefficient averaged over all exposures. This was done separately for the DS and TRES spec-

**Table 2.** Heliocentric radial velocity measurements of GW Ori.

HJD (2,400,000+)	RV (km s <sup>-1</sup> )	$\sigma_{\text{RV}}$ (km s <sup>-1</sup> )	$\phi_{\text{in}}$	$\phi_{\text{out}}$
44919.0042	31.43	1.88	0.2480	0.9360
45301.8865	26.55	1.28	0.8338	0.0274
45336.7941	24.43	1.26	0.9784	0.0358
45708.7038	30.41	1.79	0.5187	0.1246
45709.6058	35.22	1.14	0.5225	0.1248

NOTE—Observations up to HJD 2,454,926.6573 were obtained with the DS, and the remainder with TRES. Phases in the inner and outer orbits are represented with  $\phi_{\text{in}}$  and  $\phi_{\text{out}}$ . This table is available in its entirety in machine-readable form.

tra, using only the order centered on the Mg I b line, for consistency.

In principle these template parameters may be interpreted as estimates of the physical properties of the star. In practice, however, the narrow wavelength range ( $\sim 100$  Å for TRES, 45 Å for DS) limits the analysis by introducing a degeneracy between temperature, surface gravity, and metallicity such that a match of nearly equal quality is obtained by slightly increasing or decreasing these template parameters in tandem. We therefore made the reasonable assumption that GW Ori has solar metallicity, as expected for young stars, and we held  $\log g$  fixed at a range of values between 2.5 and 4.0, varied in steps of 0.5, and solved only for  $T_{\text{eff}}$  and  $v \sin i$ . The best fit was found for  $\log g = 3.0$ , for both the DS and TRES spectra, and the resulting temperatures and rotational broadenings were very similar: 5180 K and  $43 \text{ km s}^{-1}$  for DS, and 5210 K and  $44 \text{ km s}^{-1}$  for TRES. For the remainder of the paper we adopt consensus values of  $T_{\text{eff}} = 5200 \pm 200$  K and  $v \sin i = 44 \pm 2 \text{ km s}^{-1}$ . Because of the strong dependence of temperature on the adopted surface gravity (and metallicity) we cannot rule out a bias in  $T_{\text{eff}}$ , which may also have a contribution from veiling (not considered in our templates), if significant in the spectral region analyzed. Radial velocities were based on a template with parameters nearest to those reported above ( $T_{\text{eff}} = 5250$  K,  $v \sin i = 40 \text{ km s}^{-1}$ ,  $\log g = 3.0$ ); they are listed in Table 2 in the heliocentric frame along with our uncertainty estimates from XCSAO. The average internal errors for the DS and TRES velocities are  $1.41$  and  $0.98 \text{ km s}^{-1}$ , respectively.

<sup>1</sup> IRAF is distributed by the National Optical Astronomy Observatories, which are operated by the Association of Universities for Research in Astronomy, Inc., under cooperative agreement with the National Science Foundation.

### 2.3. Time-series Photometry

From a combination of ongoing photometric surveys and archival observations, we have assembled  $\sim 30$  years of high cadenced photometric observations. In this section we present our photometric data and analysis. See Figure 3 for the full  $\sim 35$  year light curve of GW Ori.

#### 2.3.1. Maidanak Observatory

#### 2.3.2. KELT

The Kilodegree Extremely Little Telescope (KELT) project uses two telescopes to survey over 70% of the entire sky searching for transiting planets around bright stars ( $8 < V < 11$ ). The telescopes, located in Sonoita, AZ (KELT-North) and Sutherland, South Africa (KELT-South), have a 42mm Mamiya 645-series wide-angle lens resulting in a  $26^\circ \times 26^\circ$  field-of-view (FOV), and a  $23''$  pixel scale. Additionally, both telescope use a broad  $R$ -band filter. KELT observes using a paramount ME German equatorial mount with a  $180^\circ$  meridian flip. Therefore KELT observes in a “East” and “West” orientation. The telescope optics are not perfectly axisymmetric, and therefore, the PSFs of a star changes from one orientation to the other. The east and west observations are treated as separate telescopes through the entire data reduction process. See Siverd et al. (2012) and Kuhn et al. (2016) for a detailed description of the KELT observing strategy and reduction process. GW Ori is located in KELT-South field 05 ( $\alpha = 06\text{hr } 07\text{m } 48.0\text{s}$ ,  $\delta = +3^\circ 00' 00''$ ) and observed from UT 2010 February 28 until UT 2015 April 09, obtaining 2889 observations after reduction. KELT-South achieves a median per-point error of 0.005 mag on GW Ori.

#### 2.3.3. ASAS

Using two observing location, in Las Campanas, Chile and Haleakala, Maui, the All-Sky Automated Survey (ASAS) project was designed to observe the entire sky down to an optical magnitude of 14. The two observatory setups each contained a wide-field Minolta 200/2.8 APO-G telephoto lenses with a  $2\text{K} \times 2\text{K}$  Apogee CCD and both observed simultaneously in  $B$ - and  $V$ -band. The telescope and camera set up correspond to a  $8.8^\circ \times 8.8^\circ$  field-of-view. ASAS observed GW Ori in the  $V$ -band from UT 2001 March 11 until UT 2009 November 29, obtaining 480 observations with a median per-point error of 0.036 mag.

#### 2.3.4. ASAS-SN

Focused on the discovery and characterization of SuperNovae, the the All-Sky Automated Survey for SuperNovae (ASAS-SN, Shappee et al. (2014)) surveys the entire sky down to  $V \sim 17$  mag every  $\sim 2$  days. Located

at the Mount Haleakala, Hawaii and the Cerro Tololo InterAmerican Observatory (CTIO) in Chile, each observatory location hosts four 14-cm Nikon telephoto lenses with a  $2\text{k} \times 2\text{k}$  thinned CCD. The telescopes have a  $4.5 \times 4.5$  degree field-of-view and a  $7''.8$  pixel scale. The Las Cumbres Observatory (LCO) hosts the ASAS-SN units in both locations (Brown et al. 2013). ASAS-SN obtained 799 observations of GW Ori from UT 2014 December 16 until UT 2017 March 15, with a typical per point error of 0.01 mag.

#### 2.3.5. Photometric Analysis

Using the Lomb-Scargle (LS) periodicity search algorithm (Lomb 1976; Scargle 1982) within the VARTOOLS analysis package (?), we searched for periodic variability in the high cadenced KELT observations. Specifically, we remove the eclipses shown in Table 2.4 from the KELT data and searched for a periodic signal from 1.1 to 100 days. The top two periods we recover are 74.798 and 2.931 days. See Figure 5 for the phase-folded lightcurves. Additionally, we remove the KELT observations and phase the  $V$ -band observations from ASAS, ASAS-SN, and Maidanak to our derived orbital periods of 241.79 and 4121.12 days. We find no convincing coherent signal at the  $\sim 242$  days but the photometric observations phased to the  $\sim 4121$  day period show a coherent sinusoidal variability with a peak-to-peak amplitude of  $\sim 0.15$  mag.

#### 2.4. Catalog of Photometric Eclipses

### 3. ANALYSIS AND RESULTS

#### 3.1. A Reconstruction of the Disk Velocity Field

We use the spatially and spectrally resolved molecular line emission observed with ALMA to tomographically reconstruct the disk velocity field and make a dynamical measurement of the total stellar mass. We follow the forward modeling procedures described by Czekala et al. (2015, 2016) using the associated open-source software package *DiskJockey*.<sup>2</sup>

The basis of the parametric physical model adopted in this approach is a radial surface density profile,  $\Sigma(r)$ , designed to mimic a simple theoretical description for a viscous accretion disk (Lynden-Bell & Pringle 1974; Hartmann et al. 1998). It decreases like  $1/r$  interior to a characteristic radius  $R_c$ , and has an exponential taper  $e^{-r/R_c}$  at larger radii. The vertical distribution ( $z$ -direction) of these densities is controlled by the disk temperatures. To convert the total gas densities to molecule-specific values, we start with baseline

<sup>2</sup> Available under an MIT license at <https://github.com/iancze/DiskJockey>.

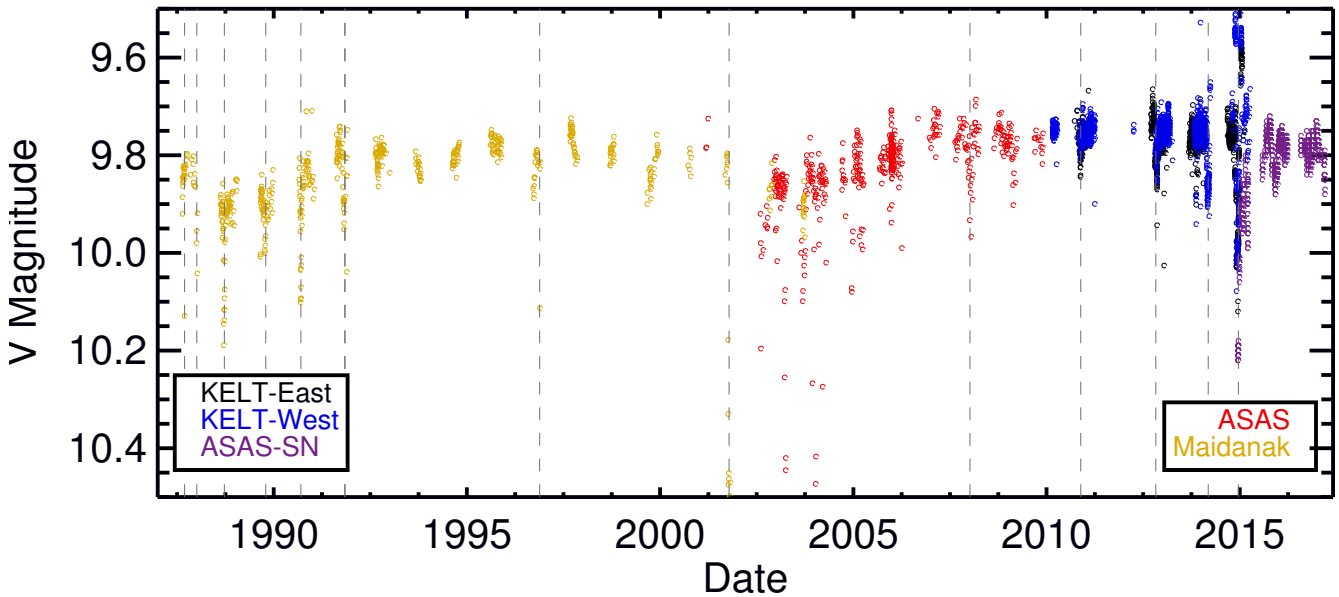


**Figure 3.** The KELT East (black), KELT West (blue), ASAS (red), ASAS-SN (purple), and  $V$ -band observations from Grankin et al. (yellow) photometric observations of GW Ori from 1987 until mid 2017. All photometric observations displayed here are in the  $V$ -band (ASAS, ASAS-SN, and Grankin et al.) or a broader filter (KELT). To place all photometric data on the same scale, we assume the  $V$ -band observations as the photometric standard and apply a vertical offset to the KELT observations to align them where they overlap. We do not otherwise correct for the filter differences. The gray vertical lines represent the time of the identified eclipses.

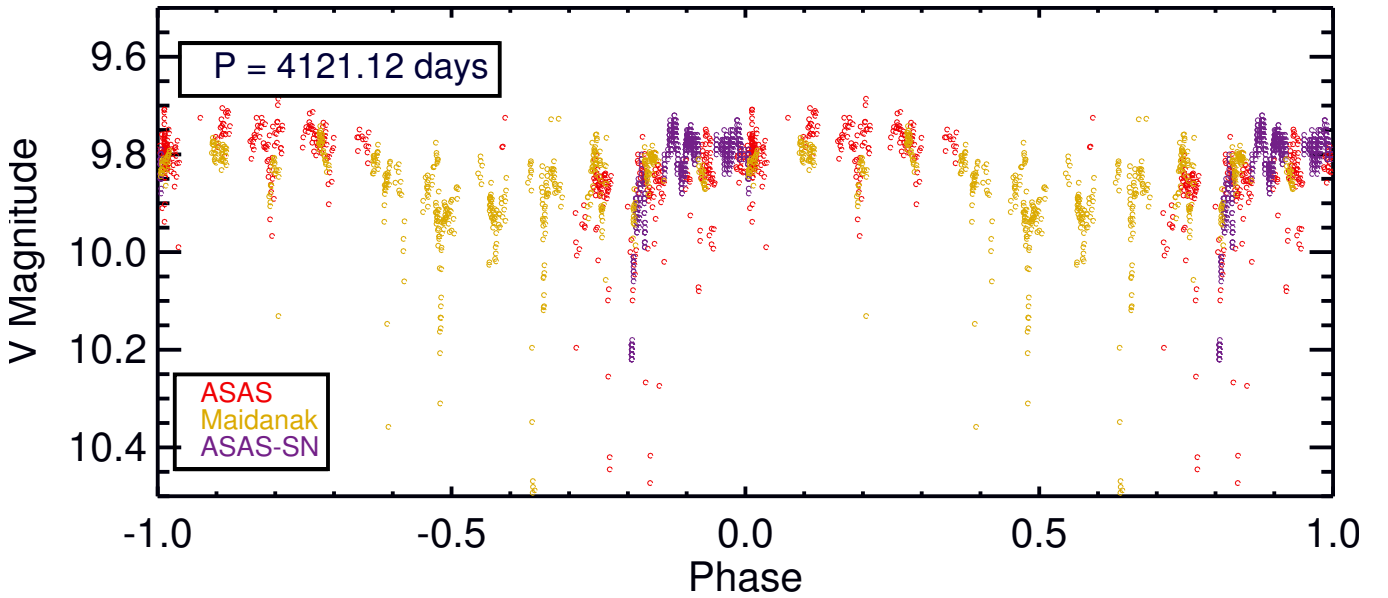


**Figure 4.** The ASAS (red), ASAS-SN (purple), and Maidanak (yellow)  $V$ -band photometric observations of GW Ori phased to  $\sim 4121$  days, the derived orbital period of the outer companion.

abundances that are representative of the cold molecu-

lar interstellar medium:  $[\mathrm{H}_2/\mathrm{gas}] = 0.8$ ,  $^{12}\mathrm{CO}/\mathrm{H} =$

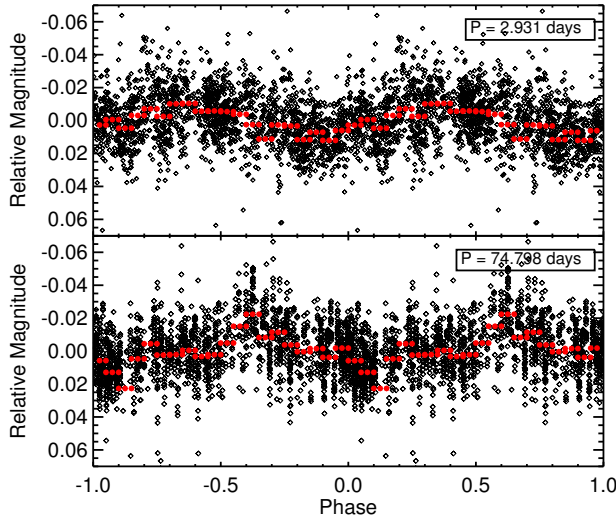


**Figure 5.** The KELT photometric observations of GW Ori, with the three eclipses removed, phased to the 2.931 (Top) and 74.798 (Bottom) day periods recovered from our LS analysis.

**Table 3.** V-band Photometric Eclipse Catalog

Start JD	End JD	Duration days	Depth mmag	Telescope
2447043	2447056	13	600	Maidanak
2447153	2447179	26	300	Maidanak
2447418	2447435	17	450	Maidanak
2447809	2447824	15	130	Maidanak
2448137	2448162	25	300	Maidanak
2448545	2448586	41	150	Maidanak
$\geq 2450399$	$\leq 2450414$	$\leq 15$	300	Maidanak
2452184	$\geq 2452209$	$\geq 25$	750	Maidanak
2454445	2454502	57	100	ASAS
2455507	2455535	28	60	KELT
2456212	2456248	36	110	KELT
2456709	2456742	33	150	KELT
2456989	2457032	$\leq 43$	$\geq 250$	KELT

$7.5 \times 10^{-5}$ ,  $[^{12}\text{CO}/^{13}\text{CO}] = 69$ , and  $[^{12}\text{CO}/\text{C}^{18}\text{O}] = 557$  (e.g., Henkel et al. 1994; Prantzos et al. 1996).

The disk kinematics are assumed to be Keplerian and dominated by the total stellar mass  $M_{\text{tot}}$ , with a velocity field that appropriately accounts for the two-dimensional distribution of the emitting layer (see Rosenfeld et al. 2013). The line-spread function is char-

acterized with a width defined by the quadrature sum of thermal and non-thermal ( $\xi$ ; presumably turbulent) contributions. For any physical structure specified by these 6 parameters,  $\{\Sigma_c, R_c, T_{10}, q, M_{\text{tot}}, \xi\}$ , we solve the molecular rate equations (assuming LTE) and ray-trace the associated emission into a set of high resolution channel maps using the radiative transfer package RADMC-3D (Dullemond 2012). That ray-tracing requires that we specify 3 additional geometric parameters: the disk inclination to the line-of-sight ( $i_{\text{disk}}$ ), the position angle of the disk rotation axis projected on the sky ( $\varphi$ ), and the LSRK systemic radial velocity ( $v_r$ ). Hereafter, we term this parameterization the “standard” model. The model channel maps are then Fourier transformed and sampled at the same spatial frequencies observed by ALMA. The model quality with respect to the observed visibilities is evaluated with a  $\chi^2$  likelihood function that incorporates the nominal visibility weights. We assume flat priors on all parameters except for  $i_{\text{disk}}$ , where we adopt a simple geometric prior (the disk angular momentum vector  $\mathbf{h}_{\text{disk}}$  is distributed uniformly on a sphere, e.g.; Czekala et al. 2016). We adopt a fixed distance to GW Ori of  $d = 388$  pc (Kounkel et al. 2017) to make the problem more computationally tractable; we discuss the effects of this assumption in Section 3.4. The posterior distribution of these parameters is explored using Markov Chain Monte Carlo simulations with the affine invariant ensemble sampler proposed by Goodman & Weare (2010), as implemented in the emcee code (Foreman-Mackey et al. 2013) and ported to the Julia programming language, which we include in DiskJockey.

Compared to our previous similar work, the modeling of GW Ori is considerably more computationally intensive. This is primarily a consequence of the large physical size of the disk, which makes the ray-tracing step substantially more time-consuming. The inference for an individual spectral line takes  $\sim 10,000$  CPU hours parallelized across 26 cores on the Harvard Odyssey Cluster. Given that restriction and the fact that the  $^{12}\text{CO}$  line is clearly contaminated by local cloud material, we restrict our analysis to *independent* inferences of the model parameters based on the  $^{13}\text{CO}$  and  $\text{C}^{18}\text{O}$  data only. For computational expediency we only model the data averaged to 25 channels of  $0.4 \text{ km s}^{-1}$  width. Experiments modeling a subset of the channels at higher resolution (e.g., every third channel) did not yield a significantly different result.

The inferred parameter values corresponding to the measurements of each spectral line are summarized together in Table 4. A comparison of the data and the best-fit models (and associated residuals) is presented

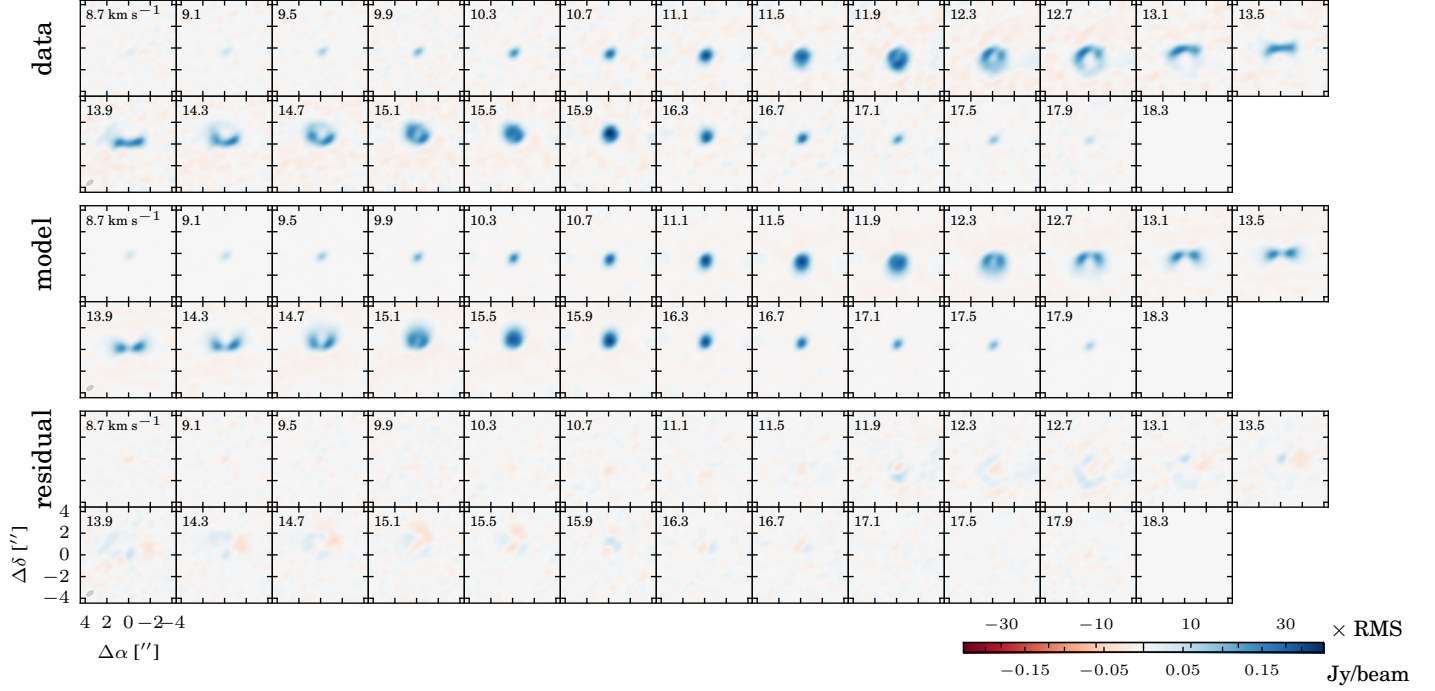


**Figure 6.** A comparison of the observed channel maps of the  $^{13}\text{CO}$  line emission (top) with a best-fit model (middle; constructed from a synthetic visibility set based on the inferred parameters listed in Table 4 and then imaged in the same way as the data) and the associated residuals (bottom; the imaged data–model residual visibilities). The annotation is the same as in Fig. 2.

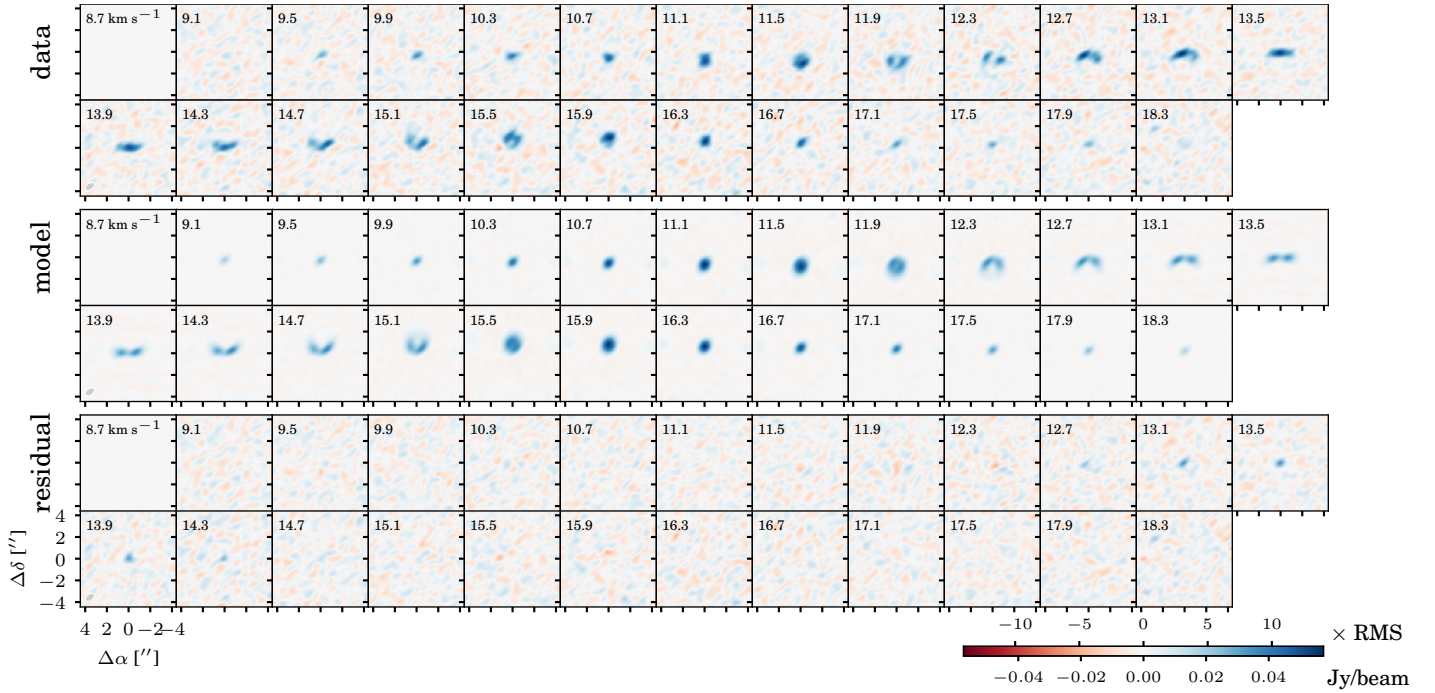


**Figure 7.** A comparison of the observed channel maps of the  $\text{C}^{18}\text{O}$  line emission (top) with a best-fit model (middle; constructed from a synthetic visibility set based on the inferred parameters listed in Table 4 and then imaged in the same way as the data) and the associated residuals (bottom; the imaged data–model residual visibilities). The annotation is the same as in Fig. 2.

in the form of channel maps in Figures 6 and 7 for  $^{13}\text{CO}$  and  $\text{C}^{18}\text{O}$ , respectively. While overall the models

successfully reproduce the observed emission, there are some interesting residuals. Namely, an excess of emis-

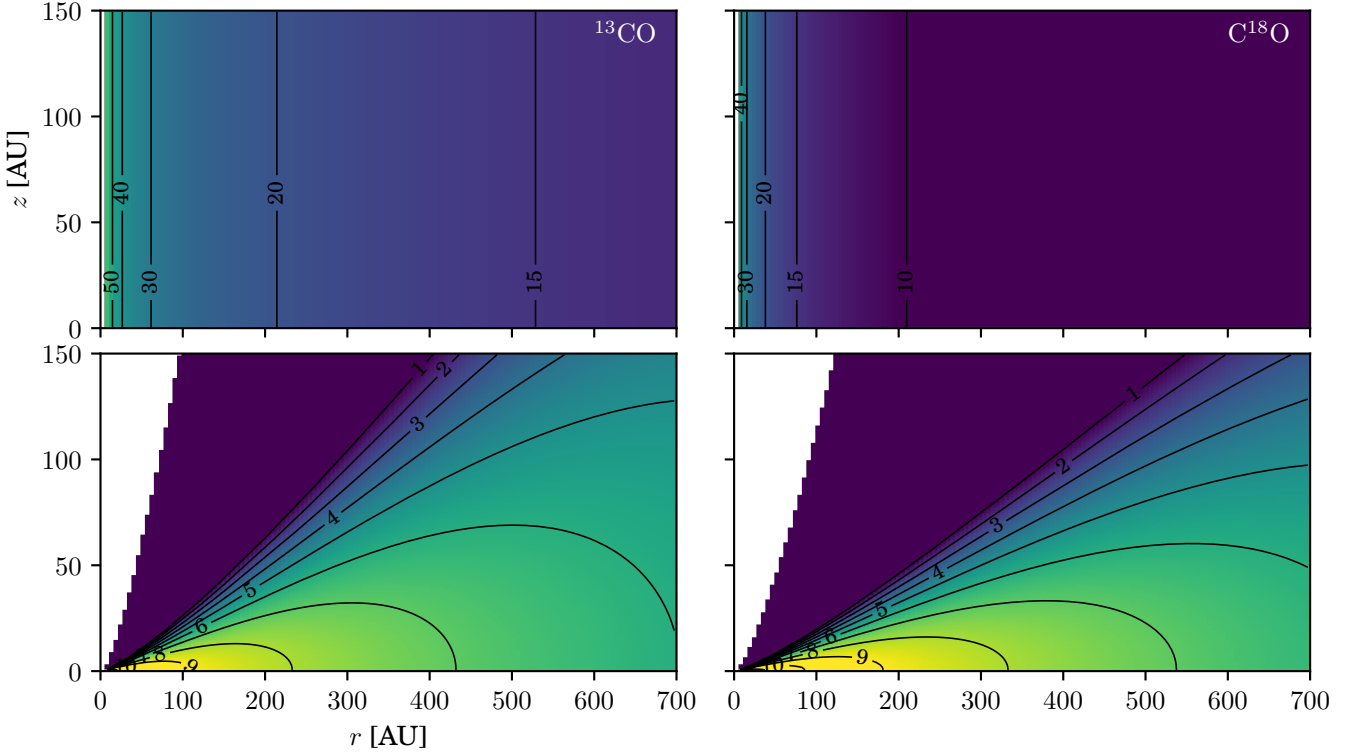


**Figure 8.** The maximum likelihood 2D temperature (top) and density (bottom) disk structures inferred using the  $^{13}\text{CO}$  (left) and  $\text{C}^{18}\text{O}$  (right) transitions. The temperature contours are in units of K. The density plots show the total gas density ( $\rho_{\text{gas}}$ ) and are in units  $\log_{10} \text{cm}^{-3}$ . The color scales are normalized to the same limits for both transitions.

**Table 4.** Inferred Disk Model Parameters

Parameter	$^{13}\text{CO}$	$\text{C}^{18}\text{O}$
$M_*$ [ $M_\odot$ ]	$5.28 \pm 0.06$	$5.38 \pm 0.23$
$r_c$ [AU]	$237 \pm 5$	$151 \pm 21$
$T_{10}$ [K]	$51 \pm 2$	$32 \pm 4$
$q$	$0.308 \pm 0.012$	$0.378 \pm 0.037$
$\log_{10} M_{\text{disk}}$	$\log_{10}[M_\odot]$	$-1.69 \pm 0.02$
$\xi$ [ $\text{km s}^{-1}$ ]	$0.59 \pm 0.01$	$0.37 \pm 0.03$
$i_d$ [ $^\circ$ ]	$137.7 \pm 0.3$	$135.2 \pm 1.4$
PA <sup>a</sup> [ $^\circ$ ]	$90.7 \pm 0.1$	$90.5 \pm 0.6$
$v_r$ [ $\text{km s}^{-1}$ ]	$13.651 \pm 0.003$	$13.649 \pm 0.015$
$\mu_\alpha$ [ $''$ ]	$-0.004 \pm 0.002$	$-0.028 \pm 0.010$
$\mu_\delta$ [ $''$ ]	$-0.044 \pm 0.002$	$-0.051 \pm 0.008$

<sup>a</sup>For comparison with the stellar orbits, we note that the position angle of the ascending node  $\Omega_{\text{disk}}$  is  $90^\circ$  offset from our PA convention, i.e.  $\Omega_{\text{disk}} = \text{PA} + 90^\circ \approx 180.6^\circ$ .

NOTE—The 1D marginal posteriors are well-described by a Gaussian, so we report symmetric error bars here.

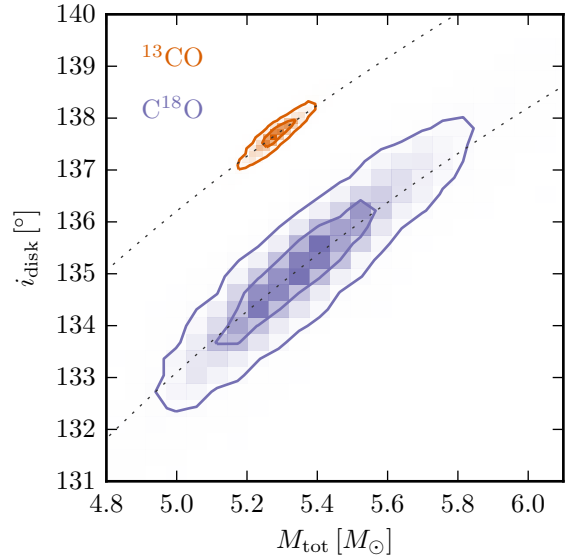


**Figure 9.** Posterior distributions for the model parameters fit to the  $^{13}\text{CO}$  and  $\text{C}^{18}\text{O}$  data independently, showing 1 and  $2\sigma$  contours. Dashed lines indicate constant values of  $M_{\text{tot}} \sin^2 i_{\text{disk}}$ .

sion in the center of the disk for the channels between

$13.1 - 14.3 \text{ km s}^{-1}$ , seen in both  $^{13}\text{CO}$  and  $\text{C}^{18}\text{O}$ . We will return to a discussion of a potential origin in Section 4.

Motivated by the presence of the aforementioned residuals, we explored more sophisticated disk models, including a model with a vertical temperature gradient and CO depletion due to freeze-out and photodissociation (after Rosenfeld et al. 2013), as well as a flexible temperature model parameterized to mimic more sophisticated (and computationally expensive) protoplanetary disk models (Kamp & Dullemond 2004; Jonkheid et al. 2004). However, we found that neither of these models resulted in a more satisfactory fit to the data as measured by visual inspection and the Akaike information criterion (AIC). Encouragingly, however, they still yielded similar estimates of  $M_{\text{tot}}$  as the standard model, which gives us confidence that the disk-based dynamical mass is moderately robust to choice of parameterization for the temperature and density structures.

Using the standard model, the inferred physical structures inferred from each line are in mild disagreement, as might be expected for this simple parameterization. To illustrate these differences, we plot the 2D temperature and density profiles inferred from each transition in Figure 8. We attribute these differences to the different layers of the disk probed by the  $^{13}\text{CO}$  and  $\text{C}^{18}\text{O}$  transitions. In Figure 9, we plot the marginalized posteriors for both transitions in the  $\{M_*, i_{\text{disk}}\}$ -plane. Interestingly, the different transitions deliver different inclinations at a statistically significant level ( $\Delta i_{\text{disk}} \approx 2.5^\circ$ ), which we attribute to the previously mentioned model deficiencies and the fact that the  $^{13}\text{CO}$  and  $\text{C}^{18}\text{O}$  transitions probe different layers in the disk. This difference is potentially concerning because biases in the measurement of disk inclination have the greatest potential to affect the inference of  $M_{\text{tot}}$ . With more computational power, it would be worthwhile to explore a joint fit to both transitions, to see if a single disk structure could adequately fit both transitions simultaneously. Nevertheless, both transitions yield consistent constraints on the total stellar mass, which is the most relevant parameter to our stated goals. We believe that the robustness of the dynamical mass technique is primarily because the kinematic morphology of the line emission (i.e., the location of the emission in R.A., Dec., and radial velocity space) is not strongly dependent on the exact temperature and density structure of the disk, but is rather a strong function of  $M_{\text{tot}}$  and  $i_{\text{disk}}$ , and when the disk is spatially resolved, the dependence on  $i_{\text{disk}}$  is diminished. We combine the inferred total masses from  $^{13}\text{CO}$  and  $\text{C}^{18}\text{O}$  in a weighted mean to get  $M_{\text{tot}} = 5.29 \pm 0.06 M_\odot$ . The uncertainty in the distance to GW Ori ( $388 \pm 5 \text{ pc}$ ; Kounkel et al. 2017) linearly translates into a mass uncertainty,

and so we convolve an additional 1.3% mass uncertainty with this posterior to get  $M_{\text{tot}} = 5.29 \pm 0.09 M_\odot$ , which we adopt as our reported total mass estimate. Because the inferred disk inclinations are mutually inconsistent, we adopt a weighted average for the mean inclination and assume a large systematic uncertainty, resulting in a final estimate of  $i_{\text{disk}} = 137.6 \pm 2.0^\circ$ .

### 3.2. Disentangling the GW Ori Double-lined Spectroscopic Binary

At optical wavelengths, GW Ori clearly appears to be a *single-lined* spectroscopic binary, despite full coverage of the 240 day inner period at moderate to high SNR (Mathieu et al. 1991; Fang et al. 2014). In this context, the Berger et al. (2011) H-band detections of the secondary and tertiary stars at favorable flux ratios ( $f_B/f_A = 0.57 \pm 0.05$ , and  $f_C/f_A = 0.23 \pm 0.01$ ) were rather puzzling, since such a bright secondary companion should have detectable signatures in the optical spectra. We originally embarked on a search for these signatures using the then-under-development PSOAP spectroscopic disentangling package (Czekala et al. 2017), with a strong assumption that these spectral signatures must be at or near the detection limit (e.g.,  $q_{\text{in}} \lesssim 0.2$ ), since they had not been seen in previous analyses. Our preliminary results hinted at the detection of a secondary spectrum, but with mass ratios much larger than what we had expected ( $q_{\text{in}} > 0.5$ ). Because the code was still under development at that time, we discounted these initial results as spurious and possibly the result of contamination by stellar variability. To our excitement, however, shortly thereafter we learned that GW Ori had been revealed as a *double-lined* spectroscopic binary using targeted high resolution infrared spectroscopy (L. Prato, private communication, March 2017), but at a much larger mass ratio than we had assumed ( $q_{\text{in}} \sim 0.65$ ). Using this knowledge, we renewed our efforts to search for the secondary signature using PSOAP and targeted TODCOR analysis.

The PSOAP spectroscopic disentangling technique works as an inference framework. Given a time-series of high resolution spectroscopic observations covering the orbital phase of the binary or triple star, it simultaneously infers the intrinsic spectrum of each star along with the stellar orbit (the radial velocity of each star as a function of time). PSOAP uses Gaussian processes to model the unknown stellar spectra, providing a robust probabilistic framework by which the spectra and orbits can be inferred in a purely data-driven manner. Once disentangled, these spectra can be used to infer fundamental stellar properties by traditional analysis techniques. For more information on the mathematical

details on PSOAP please consult Czekala et al. (2017). At present, one limitation of the PSOAP framework (and Gaussian processes in general, to some extent) is the heavy computational requirement for performing the matrix calculations. This generally limits us to considering less than 20 epochs of high resolution spectra at a time.

Consequentially, this limits the complexity of the orbital model that we can use. Although it was straightforward to extend the framework to utilize a hierarchical triple orbital model and three Gaussian process components, we found that we were unable to employ enough spectroscopic epochs to sufficiently constrain the more complex orbital model. Therefore, we experimented using different subsets of the data to test our sensitivity to presence of secondary and tertiary spectral signatures. In all of these tests, we clearly detected the features of the secondary but found no solid evidence for visible spectroscopic signatures of the tertiary. We have identified possible avenues of development to expand the number of spectroscopic epochs under consideration, but this will require more development and testing beyond the scope of this paper.

While PSOAP unfortunately has a limited ability to constrain the orbital parameters of GW Ori, it can still provide disentangled spectra of the primary and secondary stars. To work around the epoch limit, we selected the 16 highest SNR spectra in the narrow date range of JD 2455826 to 2456052, which covers  $\sim 95\%$  of the inner orbital period and both quadrature phases while being minimally sensitive to the longer term radial velocity trend due to the tertiary. To converge the binary orbital model to an adequate set of orbital parameters, we use 40 Å of spectra between 5160 and 5200 Å containing many high amplitude lines, broken up into 5 Å chunks. We note that this set of orbital parameters (which we do not report) is likely incorrect, given the triple nature of the system, but since we used a narrow range of data, the predicted radial velocities of the primary and secondary should be sufficiently accurate. Using this set of orbital and Gaussian process parameters, we disentangle a wider wavelength range of data covering 5060 - 5310 Å. This overlaps with the wavelength range of a tuned CfA version of the Kurucz models, which has been used for extensive radial velocity analysis and is tuned for solar-like stars (Buchhave et al. 2012). The disentangled spectra are shown in Figure 10, overlaid with two representative Kurucz models.

In general, an inherent limitation of disentangling techniques is that they are unable to provide any information on the flux ratios of the components, they are only able to provide the relative amplitudes of the spec-

tral variations. Essentially, there emerges a degeneracy between a bright companion star with shallow spectral lines and a faint companion star with deep spectral lines. Therefore, in order to re-normalize<sup>3</sup> the disentangled spectra to compare with synthetic models, we must assume a flux ratio between the two stars.

In light of this, the process of inferring stellar parameters becomes rather difficult, especially since both GW Ori A and GW Ori B may suffer from veiling and both the re-normalization and veiling affect the “contrast” level of the spectra. Over this narrow wavelength range,  $T_{\text{eff}}$  mainly changes the depth of the lines, while  $\log g$  and  $v \sin i$  mainly change the shape and depth of the lines. Therefore, the parameters we report are merely one of many possible best fit solutions; in reality, the stellar parameters could plausibly range by  $\Delta T_{\text{eff}} \sim 500$  K,  $\Delta \log g \sim 0.5$  dex, and  $\Delta v \sin i \sim 10 \text{ km s}^{-1}$  in a correlated manner for each star, especially given uncertainties about the flux ratio and veiling.

Throughout this analysis, we were pursuing renewed radial velocity searches in tandem with TODCOR, focusing on cross-correlating with templates that closely matched the recovered spectra. By carefully selecting the matching templates and experimenting with flux ratio, we were able to resolve the formerly single-peaked cross correlation function (CCF) into a significant detection of two components. As we detail in § XX, however, the exact radial velocity solution is highly sensitive to the choice of templates and flux ratios.

### 3.3. An Updated Model of the Stellar Orbits

The discovery orbit of GW Ori by Mathieu et al. (1991), with a period of 242 days, was based on a small subset of the same spectra used here, covering slightly more than seven years. The present data set is six times larger and extends the time coverage to nearly 35 years. Mathieu et al. (1991) noted a drift in the residuals from their spectroscopic orbit that they speculated could be due to a third component, or perhaps an asymmetry in a massive circumbinary disk, causing the reflex motion of the inner binary with a period exceeding their time coverage. As our data set expanded over the years, our own preliminary spectroscopic solutions for the 242-day orbit displayed an increasingly clear periodic pattern in the residuals with a period of about 11.5 years, strongly suggesting the presence of a third body in the GW Ori system with a nearly circular orbit. Direct near-infrared

<sup>3</sup> Note that this is *not* continuum normalization in the traditional sense (e.g. dividing by a spline fit to the stellar continuum), but simply a constant scaling by a ratio defined in Czekala et al. (2017, Eqn. 32) which preserves broad scale shapes intrinsic to the spectra.

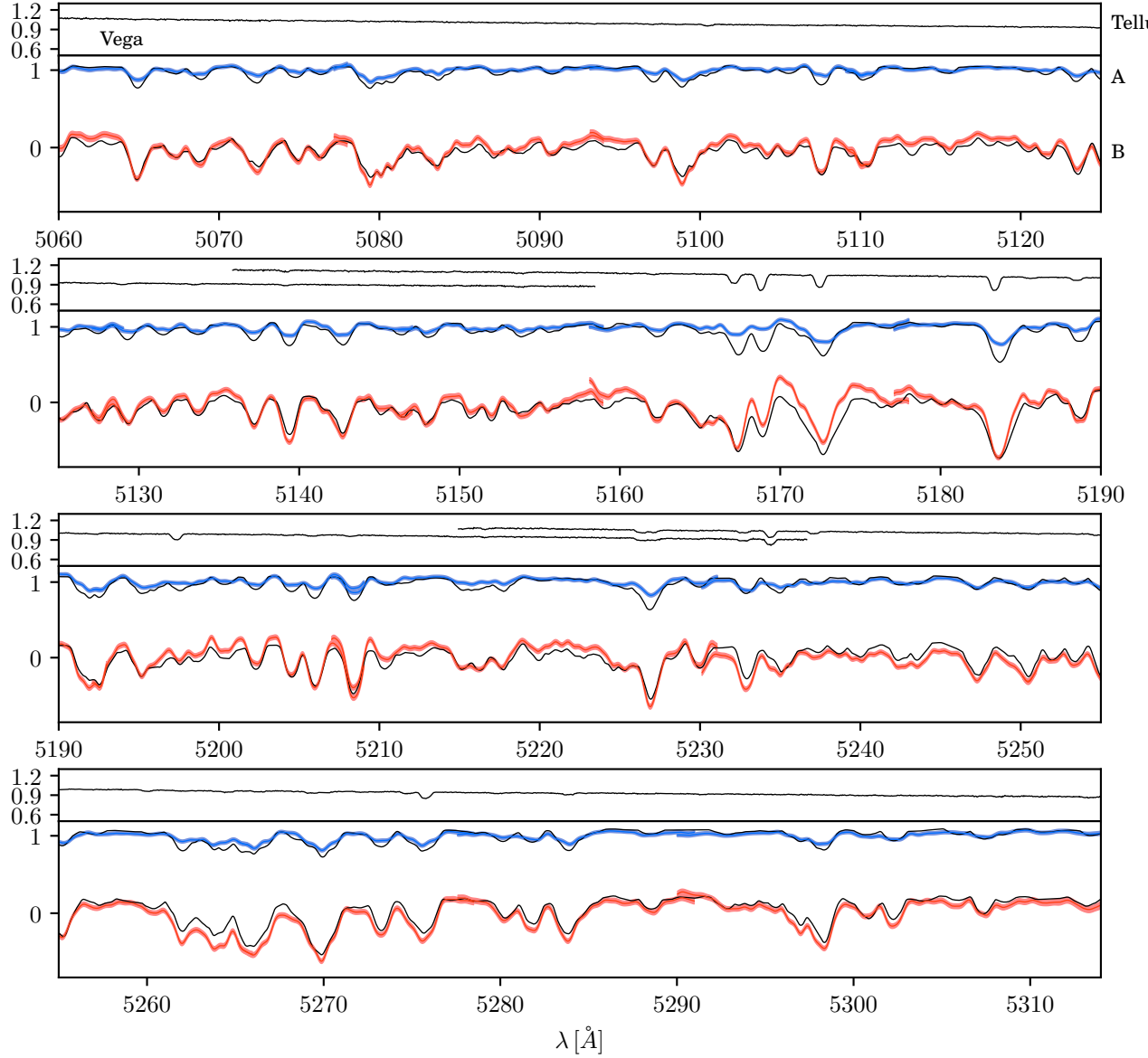


**Figure 10.** The disentangled spectra of GW Ori A and GW Ori B in blue and red, respectively. The top bar shows a spectrum of Vega, to demonstrate that this wavelength band is free from any telluric line contamination. The disentangled spectra have been inversely scaled by an assumed flux ratio to bring their continuum level to 1 to facilitate better comparison to the synthetic models. Disentangled spectra at the edges of echelle orders may appear jagged (e.g.  $\sim 5160 \text{ \AA}$ ). In this figure, we have assumed  $f_B/f_A = 0.43$ . The overplotted synthetic models for the primary and secondary stars have stellar parameters  $T_{\text{eff}} = 6000 \text{ K}$ ,  $\log g = 3.0 \text{ dex}$ ,  $v \sin i = 40 \text{ km s}^{-1}$  and  $T_{\text{eff}} = 5000 \text{ K}$ ,  $\log g = 3.0 \text{ dex}$ ,  $v \sin i = 35 \text{ km s}^{-1}$ , respectively.

imaging by Berger et al. (2011) revealed the stellar nature of the third component for the first time, and also resolved the inner binary. Our extended time coverage in radial velocities now enables us to derive a robust spectroscopic orbit for the third star.

We used standard weighted non-linear least-squares techniques (e.g., Press et al. 1992) to solve for the elements of the inner and outer Keplerian orbits simultaneously, assuming the inner binary acts as a point mass in the outer orbit, and including the effects of light travel

time. Initial fits showed that a number of the measurements had very large residuals, including instances of several consecutive exposures over periods of a few days or weeks with residuals of the same sign, possibly resulting from real phenomena such as flaring or accretion events. A total of 23 such outliers were removed, and are flagged in Table 2. Might no longer be true, with the SB2 orbit. The derived elements of the inner and outer orbits are presented in Table 5, along with other proper-

ties derived from them. The residuals from our initial fit indicated our formal velocity errors are slightly underestimated, so for our final solution we have scaled them by a factor of 1.12 to achieve a reduced  $\chi^2$  of unity.

**To be updated with SB2 orbit.** The period of the inner orbit is consistent with that of Mathieu et al. (1991), and the eccentricity is insignificant, as was also found by them. On the other hand, the velocity semi-amplitude of our inner orbit,  $K_A = 3.54 \pm 0.11 \text{ km s}^{-1}$ , is significantly smaller than theirs ( $K_A = 4.7 \pm 0.3 \text{ km s}^{-1}$ ), but similar to the one by Fang et al. (2014) ( $K_A = 3.41 \pm 0.17 \text{ km s}^{-1}$ ). Graphical representations of our observations and the inner and outer orbit models as a function of orbital phase are shown in Figure 12 and Figure 13, respectively, and a representation of the full motion as a function of time is seen in Figure 11.

Due to the uncertainty in measured radial velocities due to the unknown flux ratio, we explore radial velocity fits using a “robust” likelihood advocated by Sivia & Skilling (2006, Sec. 8.3.1) as a conservative formulation for cases where the quoted uncertainty on each data point (in this case, the statistical errors from the TODCOR RV analysis) are treated as lower limits on the actual uncertainty, and have the possibility of growing by some scale factor. This likelihood has wider “tails” than the Gaussian likelihood function used in  $\chi^2$  analysis, and is less sensitive to outliers at a (minor) expense of statistical power to constrain the orbital parameters. Given the large residuals from the orbital fit, we conclude that the statistical uncertainty of each measurement is an underestimate of the true uncertainty, and that there is a large contribution from unknown systematic effects and that a more robust likelihood function is warranted until the sources of the systematic errors can be identified.

Although there are only three epochs of published astrometry in Berger et al. (2011), these points may still considerably constrain the parameter space of possible orbits. Therefore, we explore a joint RV-astrometric analysis built upon a model of the “three-dimensional orbit” following Murray & Correia (2010), which adds new model parameters like the semi-major axis, inclination, and position angle on the sky for both inner and outer orbits. For a likelihood function, we use a combination of the aforementioned robust likelihood for the radial velocity measurements and a  $\chi^2$  likelihood function for the separation and azimuth measurements. As with the disk analysis, we also use a geometric prior on the orbital inclinations. The newly constrained parameters are  $a_{\text{in}} = 1.28 \pm 0.05 \text{ au}$ ,  $i_{\text{in}} = 150.8 \pm 1.4^\circ$ ,  $\Omega_{\text{in}} = 261 \pm 12^\circ$ ,  $a_{\text{out}} = 8.94 \pm 0.30 \text{ au}$ ,  $i_{\text{out}} = 145.6 \pm 7.7^\circ$ ,  $\Omega_{\text{out}} = 285.5 \pm 8.9^\circ$ . The stellar components are  $M_A = 3.24 \pm 0.40 M_\odot$ ,  $M_B = 1.56 \pm 0.20 M_\odot$ ,  $M_C =$

$0.76 \pm 0.22 M_\odot$ , and the total mass is  $M_{\text{tot}} = 5.26 \pm 0.55$ , which is nicely consistent with that independently measured by the disk-based analysis.

Interestingly, the inner orbital plane is inferred to be misaligned with the circum-triple disk at a statistically significant level ( $i_{\text{disk}} \approx 137^\circ$ ,  $\Omega_{\text{disk}} \approx 180.6^\circ$ ), and the outer orbital plane also appears to be inconsistent with the disk inclination, as well. Using our radial velocity results and a wide range of permissible orbital elements, one would infer that at the first epoch (2003) of the Berger et al. (2011) astrometric measurements the tertiary would be moving with a large positive radial velocity (relative to the systemic velocity) and by the last epoch (2005) it would be moving at approximately the systemic velocity, suggesting that the line of nodes for the outer orbit is close to the E-W axis. Meanwhile, our disk results clearly demonstrate that the line of nodes for the disk is the N-S axis, suggesting that these orbits must be misaligned. We note that both of these claims of misalignment rest upon only three astrometric epochs, however, so we caution against overinterpreting the exact results. In the next section, we use only our newly derived radial velocity and disk modeling results to form a more conservative estimate of the relative inclinations, but also find strong evidence that the inner stellar orbit and disk are at least mildly misaligned. We advocate future astrometric monitoring of the GW Ori system to further improve the three-dimensional orbit and confirm the inclinations of the stellar orbits.

### 3.4. Joint Radial Velocity and Disk Constraints on Individual Component Masses

In this section, we combine the double-lined spectroscopic binary constraints with the constraints on the total disk mass to infer the individual stellar masses of the GW Ori system without referencing the Berger et al. (2011) astrometry. We construct a joint likelihood function with the following five parameters:  $M_A$ ,  $M_B$ ,  $M_C$ ,  $i_{\text{inner}}$ , and  $i_{\text{outer}}$ . The double-lined radial velocity constraints are sufficiently captured by the summary statistics  $M_A \sin^3 i_{\text{inner}}$ ,  $M_B \sin^3 i_{\text{inner}}$  and  $M_C \sin i_{\text{outer}} / (M_{\text{tot}}/M_\odot)^{2/3}$  and the covariances between them, which are well represented by a multivariate Gaussian distribution.<sup>4</sup> The disk constraint on the total stellar mass  $M_{\text{tot}}$  is well-represented by a Gaussian, as well. We enforce flat priors on the stellar masses and geometrical priors on the inclinations. We use the ensemble sampler MCMC (Goodman & Weare 2010;

<sup>4</sup> Note that we do not use additional constraints on  $i_{\text{inner}}$  or other derived parameters, as this would amount to double-counting the radial velocity points in the fit.

**Table 5.** Orbital elements of GW Ori.

Parameter	RV	RV + astrometry
Inner orbit		
$P$ [days] .....	$241.446 \pm 0.066$	
$\gamma$ [ $\text{km s}^{-1}$ ] .....	$+27.726 \pm 0.082$	
$\Delta v_B^a$ [ $\text{km s}^{-1}$ ] .....	?	
$K_A$ [ $\text{km s}^{-1}$ ] .....	$3.54 \pm 0.11$	
$q$ .....		
$e$ .....	$0.016 \pm 0.029$	
$i$ [deg] .....	...	
$\omega_A$ [deg] .....	$210 \pm 100$	
$\Omega^b$ [deg] .....	...	
$T_{\text{peri}}$ [HJD–2,400,000] .....	$51861 \pm 67$	
$M_A$ [ $M_\odot$ ] .....	...	
$M_B$ [ $M_\odot$ ] .....	...	
Derived properties from inner orbit		
$a_A \sin i$ [AU] .....	$0.0787 \pm 0.0024$	
$f(M)$ [ $M_\odot$ ] .....	$0.00111 \pm 0.00010$	
$M_B \sin i / (M_A + M_B)^{2/3}$ [ $M_\odot$ ] .....	$0.1036 \pm 0.0031$	
Time interval [days] .....	12574	
Time interval [cycles] .....	52.1	
Outer orbit		
$P$ [days] .....	$4187 \pm 42$	
$K_{AB}$ [ $\text{km s}^{-1}$ ] .....	$2.04 \pm 0.12$	
$e$ .....	$0.061 \pm 0.058$	
$i$ [deg] .....	...	
$\omega_{AB}$ [deg] .....	$276 \pm 48$	
$\Omega^b$ [deg] .....	...	
$T_{\text{peri}}$ [HJD–2,400,000] .....	$53560 \pm 565$	
$M_C$ [ $M_\odot$ ] .....	...	
Derived properties from outer orbit		
$a_{AB} \sin i$ [AU] .....	$0.782 \pm 0.045$	
$f(M)$ [ $M_\odot$ ] .....	$0.00364 \pm 0.00062$	
$M_C \sin i / (M_{\text{tot}}^c / M_\odot)^{2/3}$ [ $M_\odot$ ] .....	$0.1539 \pm 0.0088$	
Time interval [cycles] .....	3.0	

<sup>a</sup>We fit for a possible velocity offset between the primary and secondary radial velocities. In reality, this term should be 0, however, the non zero value likely indicates that there may be a degree of template mismatch between the stellar spectra and the synthetic spectra used as cross correlation templates.

<sup>b</sup>We follow the convention of the visual binary field and define the ascending node as the line of nodes where the secondary component (e.g., star B for the inner orbit, and star C for the outer orbit) crosses the plane of the sky moving *away* from the observer.

<sup>c</sup> $M_{\text{tot}} = M_A + M_B + M_C$ .

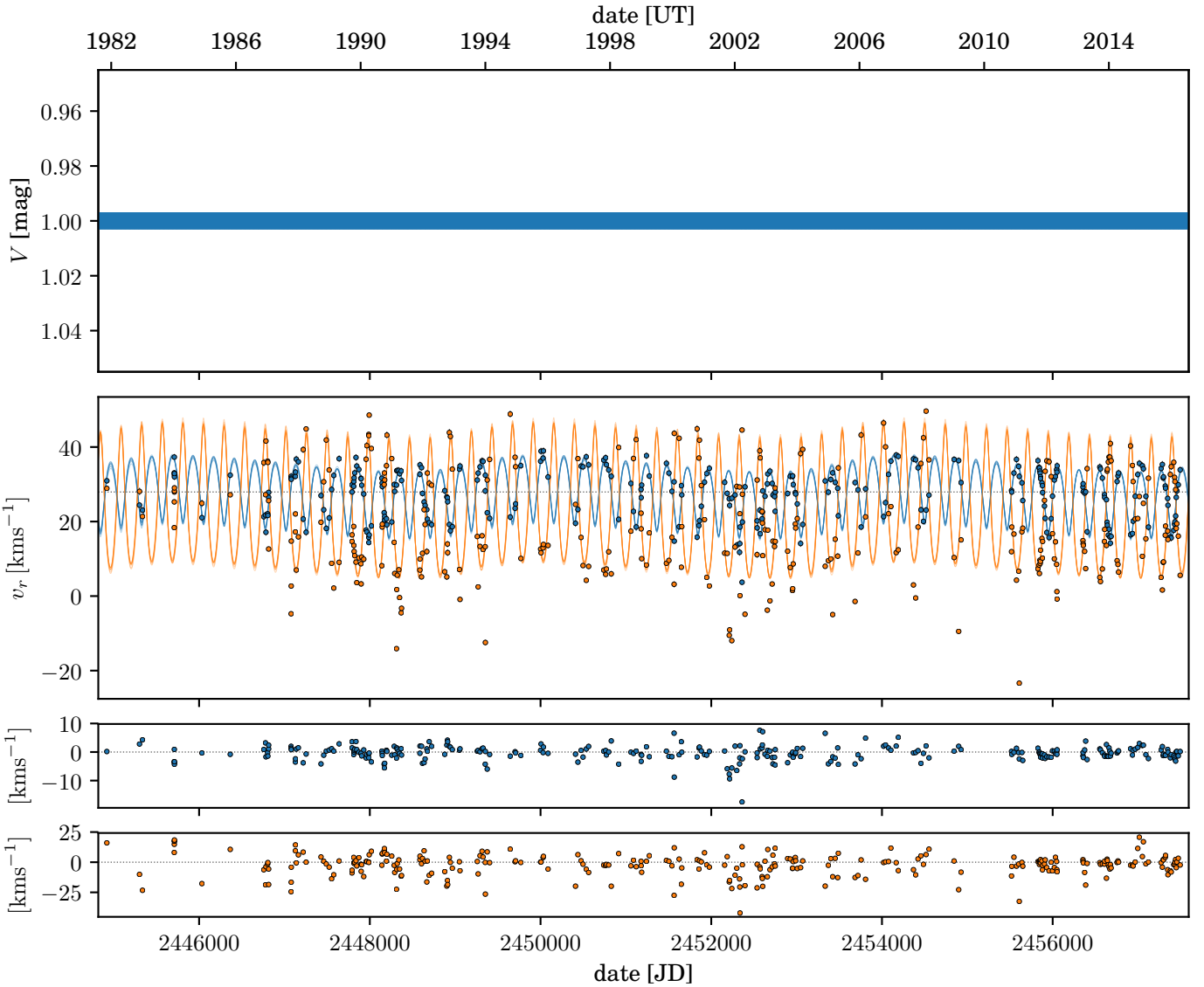


**Figure 11.** Figures for the lightcurve and radial velocities. Radial-velocity measurements of GW Ori as a function of time, and best-fit model for the triple system. The dotted line represents the center-of-mass velocity.

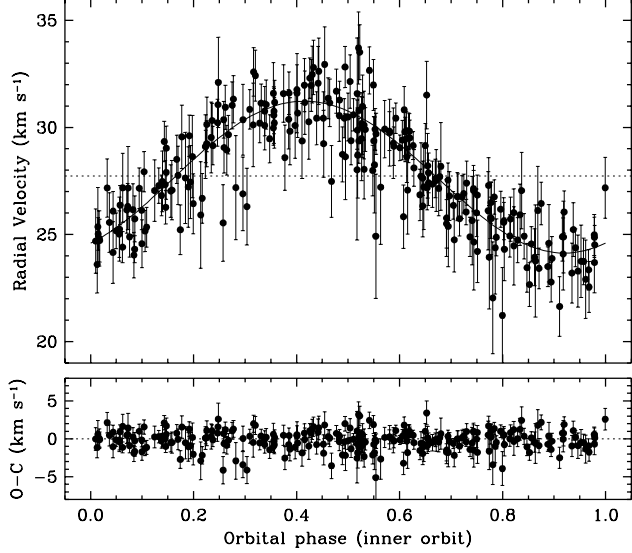


**Figure 12.** Radial-velocity measurements of GW Ori and best-fit model for the inner orbit, after subtracting the motion in the outer orbit. The dotted line in the top panel represents the center-of-mass velocity of the triple system. The bottom panel displays the residuals.

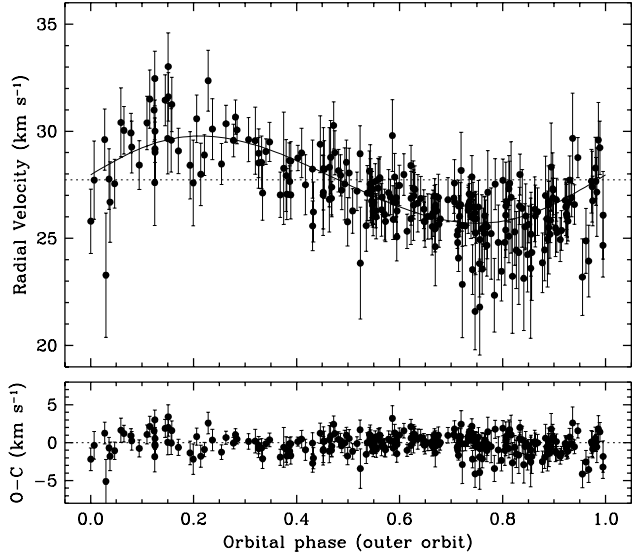


**Figure 13.** Radial-velocity measurements of GW Ori and best-fit model for the outer orbit, after subtracting the motion in the inner orbit. The dotted line in the top panel represents the center-of-mass velocity of the triple system. The bottom panel displays the residuals.

Foreman-Mackey et al. 2013) with 20 walkers to explore the posterior for 50,000 iterations, burn 25,000 iterations, and assess convergence by ensuring the Gelman-Rubin statistic (Gelman et al. 2014) is  $\hat{R} < 1.1$  for all parameters.

This analysis produces the following non-symmetric posteriors on the individual component masses and or-

**Table 6.** Joint constraints on stellar masses and orbital inclinations

Parameter	RV + astrometry	RV + disk
$M_A [M_\odot]$	$3.09^{+0.13}_{-0.59}$	
$M_B [M_\odot]$	$1.49^{+0.07}_{-0.28}$	
$M_C [M_\odot]$	$0.69^{+0.89}_{-0.17}$	
$i_{\text{inner}} [\text{deg}]$	$36.7^{+3.1}_{-0.8}$	
$i_{\text{outer}} [\text{deg}]$	$48^{+29}_{-29}$	

NOTE—The RV + astrometry values are replicated from Table 5 for comparison purposes. We note that we are not able to infer the absolute inclination of the stellar orbits directly from the radial velocity data, so there is in fact an alternate solution for the RV + disk results that yields  $i_{\text{alt}} = 180^\circ - i$ . This solution would be inconsistent with the astrometric results, however, so we opt to report the solutions with  $i \geq 90^\circ$ .

bital inclinations, summarized in Table 6. Although the RV + disk analysis is only able to constrain the inclination of the stellar orbits and not the position angle as well (as in the astrometric fit), there is still evidence that the stellar orbital plane is misaligned by the disk. If the inferred orbital inclinations are different, then this sets a lower limit on the total mutual inclination between the orbits (i.e., the angle between the angular momentum vectors of the stellar orbit and that of the disk). Even if the inclinations were inferred to be the same, if the position angles were different, the orbits would be misaligned. However, if the inclinations are not the same, then the orbits are misaligned. To highlight these findings, we overplot our newly derived constraints on the disk inclination and the stellar orbits in Figure 15.

At the lowest inclinations (nearest to edge-on,  $i = 90^\circ$ ) are the measurements for the disk in  $^{13}\text{CO}$  and  $\text{C}^{18}\text{O}$ . This is commensurate with the disk inclination measurements from ?, and so we consider these results to be robust. Next, we show the inferred inner inclination from the joint RV + disk measurements. The outer inclination is essentially unconstrained by the RV + disk fit. The fact that the RV + astrometric fit is inconsistent with this, tells us that perhaps there is unknown systematics affecting the fit.

We show that this misalignment is probable without needing to invoke the astrometric fits. There is a small range of inclinations that overlap. And, for those to indeed overlap, would require photospheric properties

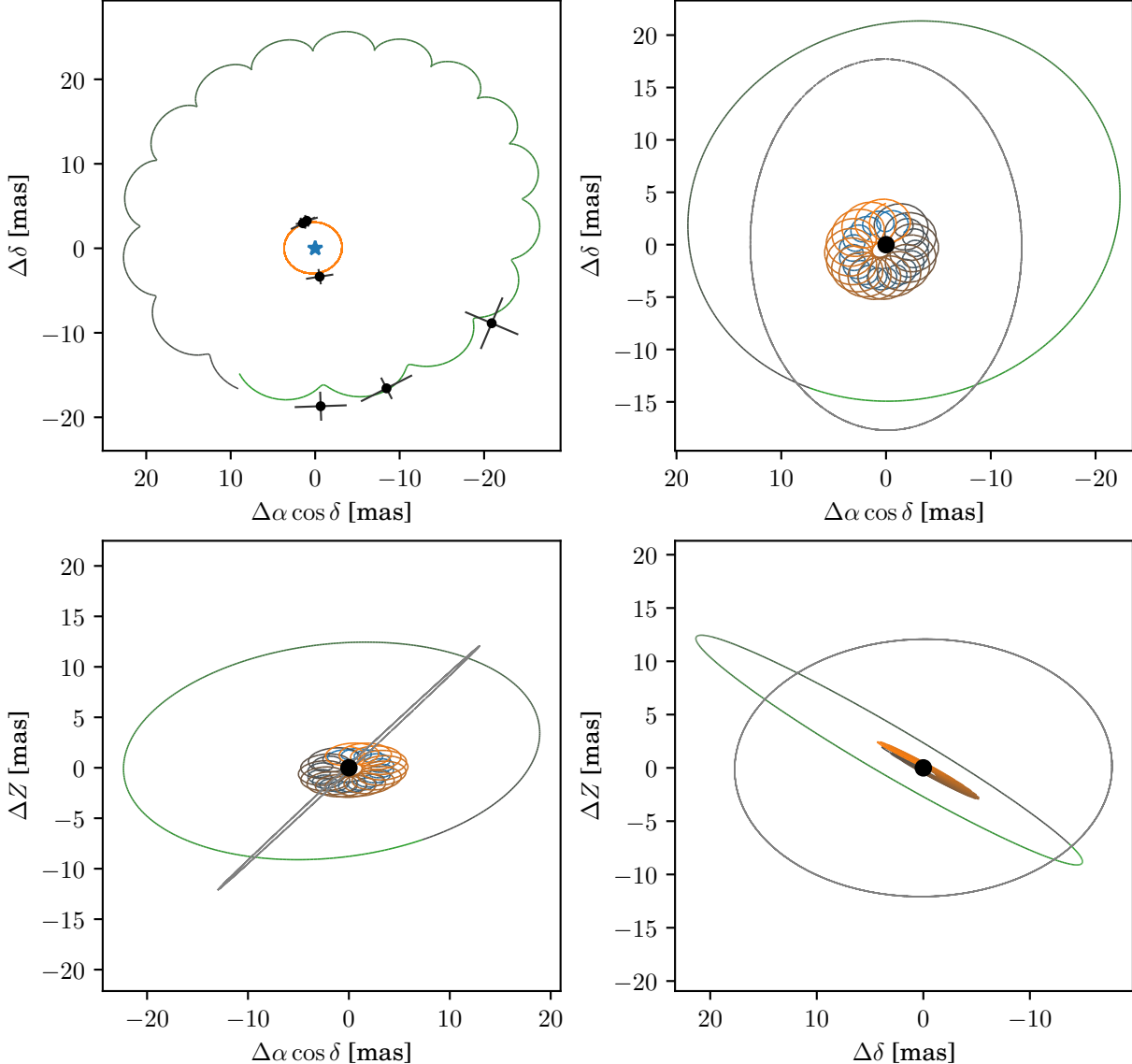


**Figure 14.** Orbits from the joint RV-astrometric fit. Orbits are shaded according to their phase, where black represents periastron, and the color hue increases with orbital phase. Top left: sky plane, relative to A. Top right, sky plane, relative to center of mass. Bottom left, looking down North axis. Bottom right, looking down East axis. Positive Z axis points towards observer. Representative disk orbit shown as grey dashed line.

which are inconsistent with our analysis. (To be detailed in next section).

#### 4. DISCUSSION

##### 4.1. The Age and Photospheric Properties of the GW Ori Stars

Pre-main sequence evolutionary models are commonly used to infer the mass and age of young stars using measurements of their photospheric properties. We perform this exercise for GW Ori A and evaluate the consistency of the model predictions with our measured dy-

namical mass. Due to the lingering uncertainties in the orbital constraints and thus the individual component masses, rather than evaluating the consistency of the pre-Main Sequence model predictions compared to our measured fundamental properties, instead we simply use the pre-Main Sequence models to guide discussion about the individual component properties and assess consistency..c

We adopt the luminosity constraints and extinction values of GW Ori as determined by Fang et al. (2014):  $L = 48 \pm 10 L_{\odot}$  and  $A_V = XX$ .

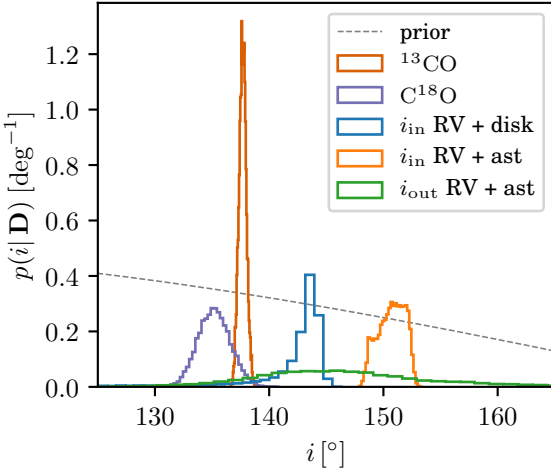


**Figure 15.** The inclination posteriors on the disk inclination, inner stellar orbit (A - B), and outer stellar orbit (AB - C), as determined from various joint fits. Because  $i_{\text{out}}$  is essentially unconstrained by the RV + disk analysis, we leave it off the plot for aesthetic reasons. The geometric prior on inclination (uniform orientation of orbits in 3D space) is shown as a thin grey dotted line.

We evaluate the concordance of the following pre-main sequence models: Choi et al. (2016) models, Dotter et al. (2008), Tognelli et al. (2011), and Siess et al. (2000). We cannot test the Baraffe et al. (2015) models because they do not include models with sufficiently massive stars. We evaluate the model predictions in a Bayesian manner, following the approach in Jørgensen & Lindegren (2005); Rosenfeld et al. (2012); Czekala et al. (2015). The models deliver (among other quantities) the photospheric properties as a function of stellar mass and age, e.g.,  $T_{\text{eff}}(M_*, \tau)$  and  $L(M_*, \tau)$ . The posterior probability distribution is found by evaluating the consistency of the model predictions for a given  $\{M_*, \tau\}$  with the measured photospheric properties by Fang et al. (2014), multiplied by any priors on  $\{M_*, \tau\}$  (in this case, flat)<sup>5</sup>. The resulting posterior probability distributions are shown in Figure 16 and are listed in Table ???. In general, all four models make similar predictions about GW Ori A,  $\langle M_A \rangle = 3.9 \pm 0.3 M_\odot$  and  $\langle \tau \rangle = 0.6 \pm 0.3 \text{ Myr}$ . We assess the probability of consistency between the model-predicted mass and our dynamical mass by evaluating  $p(M_{\text{model}} = M_{\text{dyn}}) = \int_0^\infty p_{\text{model}}(M) p_{\text{dyn}}(M) dM$ . For most models, the predicted stellar mass is significantly less than our measured dynamical mass,  $M_A = 4.40 \pm 0.18 M_\odot$ , and is consistent only at the  $2\sigma$  level.

<sup>5</sup> Our code used to perform this analysis is available under an MIT open source license here: <https://github.com/iancze/ScottiePippen>

Notably, the value of  $M_A$  predicted by our joint radial velocity and astrometric fit ( $M_A = 3.72 \pm 0.32 M_\odot$ ) is in complete agreement with the model predictions. As mentioned by Fang et al. (2014), GW Ori A is likely at an earlier evolutionary stage than Herbig Be stars, although it will eventually become one.

Berger et al. (2011) modeled the H-band visibilities of the GW Ori system measured by the IOTA/IONIC3 interferometer, and measured the positions of all three GW Ori components and their flux ratios. Their mean H-band flux ratios (computed as the weighted mean of all measurements) are  $f_B/f_A = 0.57 \pm 0.05$  and  $f_C/f_A = 0.23 \pm 0.01$ . In Figure 17, we plot the ratio of effective temperatures and the computed flux ratios in Bessel I band and 2MASS H band. Bessel I roughly corresponds to the reddest echelle orders of the TRES spectrograph that we used to search for companion spectral lines. These flux ratios are generally very small and provide an explanation for why we were unable to detect secondary or tertiary spectral lines in our searches. Moreover, this means that the excess H-band flux of the B and C components is likely due to the presence of a circumstellar disk or accretion signatures above the photospheric emission of these stars, as Berger et al. (2011) speculated. GW Ori thus presents itself as an ideal candidate for long-term high resolution infrared radial velocity monitoring to detect spectral lines from the secondary and tertiary.

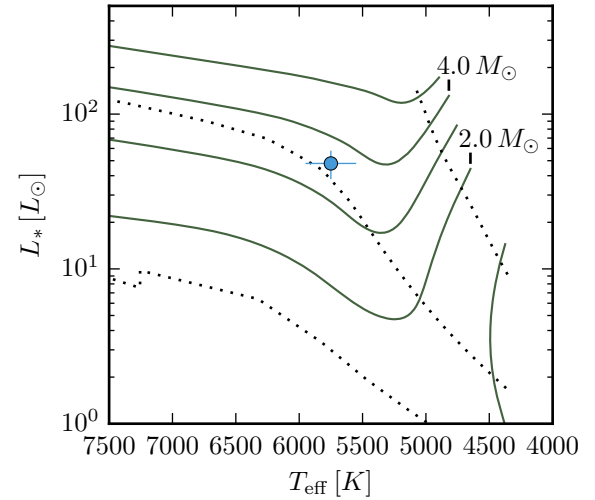


**Figure 16.** An HR diagram showing all three stars.

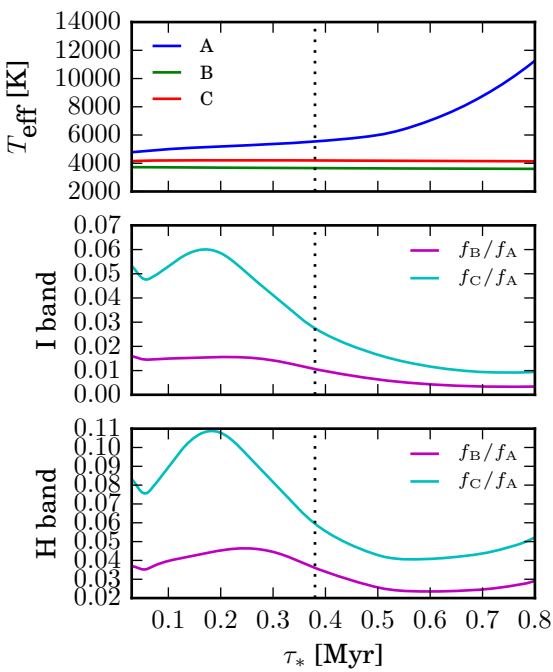


**Figure 17.** Relative photospheric properties of the GW Ori stellar components as a function of age, assuming they are coeval, predicted by the MIST pre-main sequence evolutionary models. *top:* The cool effective temperature of GW Ori A indicates that it must be a very young star ( $\tau < 5$  Myr). The nominal age of GW Ori as predicted by the MIST models is labeled as a vertical dashed line. *middle and bottom:* the predicted flux contrasts in Bessell I band and 2MASS H, respectively.

#### 4.2. The dynamic center of the GW Ori system

#### 4.3. The GW Ori triple system in context

#### 5. SUMMARY AND CONCLUSIONS

- Derived a dynamical mass for GW Ori
- Derived a new SB2 orbit for the stars, and disentangled spectra
- Compared the mutual inclinations for the disk and the stellar orbits
- Evaluate the concordance between stellar properties and PMS models
- Published lightcurve w/ eclipse analysis
- Placed system in context of triple systems
- Placed system in context of dippers

IC acknowledges support from the Smithsonian Institution for the production of this manuscript. IC acknowledges helpful conversations with Maxwell Moe about GW Ori and related systems. SA acknowledges the very helpful support provided by the NRAO Student Observing Support program related to the early development of this project. This paper makes use of the following ALMA data: XX ALMA is a partnership of ESO (representing its member states), NSF (USA), and NINS (Japan), together with NRC (Canada) and NSC and ASIAA (Taiwan), in cooperation with the Republic of Chile. The Joint ALMA Observatory is operated by ESO, AUI/NRAO, and NAOJ. This research made extensive use of the Julia programming language (Bezanson et al. 2012) and Astropy (Astropy Collaboration et al. 2013).

#### REFERENCES

- Ansdell, M., Gaidos, E., Williams, J. P., et al. 2016a, *MNRAS*, **462**, L101
- Ansdell, M., Gaidos, E., Rappaport, S. A., et al. 2016b, *ApJ*, **816**, 69
- Astropy Collaboration, Robitaille, T. P., Tollerud, E. J., et al. 2013, *A&A*, **558**, A33
- Baraffe, I., Homeier, D., Allard, F., & Chabrier, G. 2015, *A&A*, **577**, A42
- Berger, J.-P., Monnier, J. D., Millan-Gabet, R., et al. 2011, *A&A*, **529**, L1
- Bezanson, J., Karpinski, S., Shah, V. B., & Edelman, A. 2012, ArXiv e-prints, [arXiv:1209.5145 \[cs.PL\]](https://arxiv.org/abs/1209.5145)
- Brown, T. M., Baliber, N., Bianco, F. B., et al. 2013, *PASP*, **125**, 1031
- Buchhave, L. A., Bakos, G. Á., Hartman, J. D., et al. 2010, *ApJ*, **720**, 1118
- Buchhave, L. A., Latham, D. W., Johansen, A., et al. 2012, *Nature*, **486**, 375
- Choi, J., Dotter, A., Conroy, C., et al. 2016, *ApJ*, **823**, 102
- Czekala, I., Andrews, S. M., Jensen, E. L. N., et al. 2015, *ApJ*, **806**, 154
- Czekala, I., Andrews, S. M., Torres, G., et al. 2016, *ApJ*, **818**, 156
- Czekala, I., Mandel, K. S., Andrews, S. M., et al. 2017, *ApJ*, **840**, 49
- Dolan, C. J. 2000, PhD thesis, Department of Astronomy, University of Wisconsin–Madison, 475 North Charter Street, Madison, WI 53706
- Dolan, C. J., & Mathieu, R. D. 2001, *AJ*, **121**, 2124

- . 2002, *AJ*, **123**, 387
- Dotter, A., Chaboyer, B., Jevremović, D., et al. 2008, *ApJS*, **178**, 89
- Duchêne, G., & Kraus, A. 2013, *ARA&A*, **51**, 269
- Dullemond, C. P. 2012, RADMC-3D: A multi-purpose radiative transfer tool, Astrophysics Source Code Library, [ascl:1202.015](https://ascl.net/1202.015)
- Fang, M., Sicilia-Aguilar, A., Roccatagliata, V., et al. 2014, *A&A*, **570**, A118
- Foreman-Mackey, D., Hogg, D. W., Lang, D., & Goodman, J. 2013, *PASP*, **125**, 306
- Fürész, G. 2008, Ph.D. Thesis, Univ. Szeged, Hungary
- Gelman, A., Carlin, J. B., Stern, H. S., et al. 2014, Bayesian data analysis, Vol. 2 (CRC press Boca Raton, FL)
- Goodman, J., & Weare, J. 2010, Communications in Applied Mathematics and Computational Science, **5**, 65
- Hartmann, L., Calvet, N., Gullbring, E., & D'Alessio, P. 1998, *ApJ*, **495**, 385
- Henkel, C., Wilson, T. L., Langer, N., Chin, Y.-N., & Mauersberger, R. 1994, in Lecture Notes in Physics, Berlin Springer Verlag, Vol. 439, The Structure and Content of Molecular Clouds, ed. T. L. Wilson & K. J. Johnston, 72
- Jonkheid, B., Faas, F. G. A., van Zadelhoff, G.-J., & van Dishoeck, E. F. 2004, *A&A*, **428**, 511
- Jørgensen, B. R., & Lindegren, L. 2005, *A&A*, **436**, 127
- Kamp, I., & Dullemond, C. P. 2004, *ApJ*, **615**, 991
- Kounkel, M., Hartmann, L., Loinard, L., et al. 2017, *ApJ*, **834**, 142
- Kuhn, R. B., Rodriguez, J. E., Collins, K. A., et al. 2016, *MNRAS*, **459**, 4281
- Kurtz, M. J., & Mink, D. J. 1998, *PASP*, **110**, 934
- Latham, D. W. 1992, in Astronomical Society of the Pacific Conference Series, Vol. 32, IAU Colloq. 135: Complementary Approaches to Double and Multiple Star Research, ed. H. A. McAlister & W. I. Hartkopf, 110
- Latham, D. W., Stefanik, R. P., Torres, G., et al. 2002, *AJ*, **124**, 1144
- Lomb, N. R. 1976, *Ap&SS*, **39**, 447
- Lynden-Bell, D., & Pringle, J. E. 1974, *MNRAS*, **168**, 603
- Mathieu, R. D., Adams, F. C., Fuller, G. A., et al. 1995, *AJ*, **109**, 2655
- Mathieu, R. D., Adams, F. C., & Latham, D. W. 1991, *AJ*, **101**, 2184
- Murray, C. D., & Correia, A. C. M. 2010, Keplerian Orbits and Dynamics of Exoplanets, ed. S. Seager, 15
- Najita, J., Carr, J. S., & Mathieu, R. D. 2003, *ApJ*, **589**, 931
- Nordstroem, B., Latham, D. W., Morse, J. A., et al. 1994, *A&A*, **287**, 338
- Prantzos, N., Aubert, O., & Audouze, J. 1996, *A&A*, **309**, 760
- Press, W. H., Teukolsky, S. A., Vetterling, W. T., & Flannery, B. P. 1992, Numerical recipes in FORTRAN. The art of scientific computing
- Rosenfeld, K. A., Andrews, S. M., Hughes, A. M., Wilner, D. J., & Qi, C. 2013, *ApJ*, **774**, 16
- Rosenfeld, K. A., Andrews, S. M., Wilner, D. J., & Stempels, H. C. 2012, *ApJ*, **759**, 119
- Scargle, J. D. 1982, *ApJ*, **263**, 835
- Shappee, B. J., Prieto, J. L., Grupe, D., et al. 2014, *ApJ*, **788**, 48
- Shevchenko, V. S., Grankin, K. N., Ibragimov, M. A., & Melnikov, S. Y. 1992, Information Bulletin on Variable Stars, 3746
- Shevchenko, V. S., Grankin, K. N., Mel'Nikov, S. Y., & Lamzin, S. A. 1998, *Astronomy Letters*, **24**, 528
- Siess, L., Dufour, E., & Forestini, M. 2000, *A&A*, **358**, 593
- Siverd, R. J., Beatty, T. G., Pepper, J., et al. 2012, *ApJ*, **761**, 123
- Sivia, D., & Skilling, J. 2006, Data analysis: a Bayesian tutorial.
- Tognelli, E., Prada Moroni, P. G., & Degl'Innocenti, S. 2011, *A&A*, **533**, A109
- Torres, G., Neuhäuser, R., & Guenther, E. W. 2002, *AJ*, **123**, 1701